THESIS

INDICATIONS OF COMPLEX LITHOSPHERIC STRUCTURE AROUND THE CHEYENNE BELT IN THE WESTERN U.S. BASED ON SHEAR WAVE SPLITTING ANALYSIS

Submitted by

Ronald Millikan

Department of Geosciences

In partial fulfillment of the requirements

For the Degree of Master of Science

Colorado State University

Fort Collins, Colorado

Summer 2014

Master's Committee:

Advisor: Derek Schutt

Judy Hannah
Jay Breidt

ABSTRACT

INDICATIONS OF COMPLEX LITHOSPHERIC STRUCTURE AROUND THE CHEYENNE BELT IN THE WESTERN U.S. BASED ON SHEAR WAVE SPLITTING ANALYSIS

This study employs the method of shear wave splitting using a modified *Silver and Chan* methodology to produce constraints on the character of the upper mantle below the Cheyenne Belt suture zone (CB), North America. The CB marks the boundary between the Proterozoic Yavapai and Archean Wyoming Provinces. A previously undetected regional anisotropic fossil fabric with north trending fast axis orientations was detected in topographically low areas and interpreted produced by Proterozoic strain created during the convergence that produced the CB. Anisotropy results sub-parallel to absolute plate motion (APM) were detected in the mountainous areas. This is interpreted as caused by local post-Laramide heating of the lithosphere, which has reset Proterozoic anisotropy. This interpretation explains the complexity of shear wave splitting noted in Colorado by other studies.

ACKNOWLEDGEMENTS

I must express my sincere gratitude to my advisor, Derek Schutt, for his patience, friendship and guidance as he taught me to view the earth as a geophysicist. I would also like to thank my committee member Jay Breidt for his time, effort and statistical expertise he has brought to our research. And, of course, Judy Hannah, whose friendly face and kind demeanor the first time I came to CSU to learn about the geosciences program represented the college so well, that I quickly quit my job and enrolled. Finally I want to thank my fellow student and officemate Jamie Pierce for the friendship and long discussions about difficult geophysical concepts.

TABLE OF CONTENTS

LIST OF TABLES

LIST OF FIGURES

CHAPTER 1

1.1 Introduction

This work describes the methods and results of shear wave-splitting research performed on the Cheyenne Belt region of southern Wyoming and northern Colorado, North America. Seismic data was analyzed using the Transverse Component Minimization Method devised by *Silver and Chan* [1991] to determine subsurface anisotropic characteristics.

1.2 Organization of Thesis

This thesis follows a three-part configuration. Chapter one is intended to inform audiences unfamiliar with seismic anisotropy, seismic phase paths, and the method of shear wave splitting such that they can better appreciate this work as a whole. Chapter two is written in a form potentially acceptable for submission to a peer-reviewed journal, likely the American Geophysical Union's Journal of Geophysical Research. Chapter three offers advice for the direction of future research.

1.3 Anisotropy

A material is described as isotropic with respect to a physical property if the property shows no directional dependence. As an example, the velocity of light in glass is isotropic. Consequently, when viewing a dot on a piece of paper through glass, the dot does not change in appearance or location as the glass as rotated (Fig. 1.1A). An anisotropic substance has a physical property that is directionally dependent, like the velocity of light in the mineral calcite. In the case of calcite, two dots will be seen as the light is split into two perpendicularly polarized waves. As the calcite is rotated 360° one dot will complete a circle around the other (Fig. 1.1B). Although it is difficult to detect, the light travelling along one plane travels faster than the other.

In a similar way, parts of the earth exhibit seismic velocity anisotropy. When a shear wave encounters an anisotropic layer, it can be split into two near-perpendicular waves, one propagating faster than the other. This phenomenon, called shear-wave splitting (SWS), can be characterized through two parameters: ϕ (phi) – the azimuth of the fast plane, and δt (delta t)– the time in seconds between the arrival of seismic energy on the fast plane and its arrival on the slow plane.

Certain minerals common to the Earth's mantle exhibit anisotropy. Of these the most important is olivine (Fig. 1.2). In parts of the mantle, very roughly above 200 km depth, olivine is expected to deform through a mechanism called deformation creep, which causes the olivine grains in the mantle to align preferentially in a particular direction [*Hess*, 1964]. In many cases, olivine crystals will become oriented such that their fast axis is parallel to the primary strain axis. In this way a measurement of anisotropy in the mantle is a proxy for a measurement of the direction of strain, which may be the result of ongoing mantle flow or past episodes of deformation.

Anisotropy is also common in Earth's crust, where it can be caused by preferential alignment of cracks or minerals. Thicknesses involved in crustal anisotropy are much smaller than those in the upper mantle, so the crustal component of an anisotropic measurement is assumed to be negligible [*Long and Silver*, 2009].

1.4 Detection of Anisotropy

Of all the S wave phases, ones that travel through the Earth's outer core are particularly useful. The outer core is liquid, so it cannot support the shear stress of an S wave. When an S wave reaches the core-mantle boundary some of its energy is converted into a P wave (Fig. 1.3A). This conversion removes any information the wave may have been carrying about

anisotropy it encountered along its downward path from an earthquake's epicenter to the core. As the P wave exits the outer core some of its energy produces a new S wave containing no anisotropic information and with a known orientation related to the azimuth from the seismometer to the earthquake. When detected by a seismometer, any information about anisotropy is known to have developed when it encountered anisotropic material on its upward path from the core-mantle boundary to the seismometer. For this reason, the most common S wave phases used to detect mantle anisotropy are the SKS the SKKS and the PKS (hereafter called *KS) (Fig. 1.3B).

Seismologists often work in a coordinate system defined by the direction from the seismometer to the earthquake that produced an observed seismogram known as the back-azimuth (Figure 1.4). To enable the isolation of the energy from a *KS phase, waveforms are converted from the north, east and vertical orientation (the Global Reference Frame) recorded by a seismometer to a radial, transverse and vertical orientation (the Event-Station Reference Frame) (Figure 1.5).

As a consequence of their paths, *KS phases start their upward leg polarized in the radial plane (Figure 1.6). Detection of anisotropic material along the upward leg of the *KS phases path will occur if the material exists, and if the radial plane of the *KS phase does not align with the material's fast or slow axes (Figure 1.7). Approaches from angles not aligned with the material's fast or slow axes produce varying amounts of anisotropy with the amount of observed transverse energy maximized for approaches equiangular between the fast and slow axes i.e. 45°, 135°, 225° and 315°.

1.5 Notable Contributors to the Detection of Anisotropy

Notable contributions to the science of S phase analysis to infer mantle flow include *Turner* [1942] who documented the preferred orientations of olivine crystals during deformation; *Verma* [1960] who determined the fast and slow axes of olivine crystals; *Hess* [1964] who demonstrated that inferences about mantle flow based on anisotropy analysis can be geophysically defensible; *Vinnik et al.* [1984] who first used the SKS phase for anisotropy detection; and *Silver and Chan* [1991] who proposed the concept of lithospheric "fossil" anisotropy related to the last major regional deformation event for continental interiors.

1.6 The Silver and Chan Method

The most popular method for the study of seismic anisotropy has been the Transverse Component Minimization Method [*Silver and Chan*, 1991], often just called the Silver and Chan method. This method assumes that detected anisotropy is the result of a single flat layer of anisotropic material with a constant fast axis orientation, and that input *KS waves are vertically incident. Data are rotated from North/South and East/West components to radial and transverse components. Seismic energy on both the radial and transverse components is a positive indicator for anisotropy (unless the ray path is bent off the great circle path), much like the two dots viewed through calcite. This method then determines which values of ϕ and δt are most capable of removing all energy from the transverse component. When found, the ϕ value approximates the azimuth of the fast axis of the anisotropic material, and the δt value is the time difference between the fast and slow-polarized waves. Actual δt values are proportional to the product of the thickness of encountered anisotropic material and the degree of alignment between *KS wave's propagation direction and the material's fast axis.

The assumption that a *KS wave will only encounter a single anisotropic layer of material that has a constant fast axis orientation is a sizeable oversimplification of the earth's upper mantle. It is more likely that a *KS wave will encounter multiple layers of anisotropic material, each with varying degrees of anisotropy, and varying strikes and dips. This variety of orientation and material properties introduces considerable complexity to the *KS waveform. Synthetic waveforms demonstrate the relative simplicity of a *KS waveform altered by a single layer of anisotropic material (Fig. 1.8A), and the complexity of a *KS waveform altered by two layers of anisotropic material (Fig. 1.8B).

1.7 Study Site

Anisotropy studies using *KS data have been conducted all over the world (Fig. 1.9). The focus of this study is the Cheyenne Belt, a mid-continent suture zone in North America where subduction of oceanic lithosphere drew closer and attached 1.8 Ga island arcs to the ~ 2.5 Ga Wyoming Province (Fig. 1.10). Most of Colorado rests on the Yavapai Province, the result of the addition of these volcanic arc fragments to the growing North American continent (Fig. 1.11).

1.7.1 The Wyoming Province

The Cheyenne Belt separates the Archean Wyoming Province to the north from the Proterozoic Yavapai Province to the south. It is a Proterozoic suture zone expressed as a multi-fault, northeast striking, subvertical shear zone [*Sullivan and Beane*, 2013]. The Wyoming Craton is composed of five main subprovinces, each with a unique history (Fig. 1.12).

The Sweetwater Subprovince is at least 2.9 Ga old. It likely had an active southern margin based on recorded periods of magmatism, basin formation and deposition and shortening [*Chamberlain et al.*, 2003].

The Sierra Madre – Medicine Bow exotic block appears allocthonous to all other parts of the Wyoming Craton and was likely accreted to the southern margin of the Sweetwater Subprovince no earlier than 2.62 Ga [*Chamberlain et al.*, 2003].

The Hartville – Black Hills block formed to the east of the Sweetwater Subprovince and is different than the rest of the Wyoming Province with both Archean and Proterozoic basement rock. It accreted to the southeastern margin of the Sweetwater Subprovince no earlier than 2.55 Ga [*Chamberlain et al.*, 2003].

These subprovinces, together with the Bighorn and the Montana Metasedimentary subprovinces to the north, compose the Wyoming Craton, which together with the Slave, Rae, Hearne and Superior cratons make up the Precambrian Laurentian Shield (or Laurentia) [*Whitmeyer and Karlstrom*, 2007]. Between 2.45 – 2.1 Ga Laurentia was a part of the supercontinent Kenorland, along with the continents Baltica, Australia and Kalahari [*Pesonen et al.*, 2003].

Rifting, possibly related to the breakup of Kenorland, along the southern margin of the Wyoming Craton, affecting the three Wyoming Craton subprovinces contacting the Cheyenne Belt, occurred between 2.1 and 2.0 Ga forming a passive margin [*Pesonen et al.*, 2003], [*Chamberlain et al.*, 2003]. This passive margin accumulated ~300 Ma of sediments before its activation and closure [*Yuan and Dueker*, 2005].

1.7.2 The Yavapai Province

Formation of the next supercontinent might be associated with the subduction south of the Wyoming Craton that produced accretion of the Yavapai Province. Between 1.83 – 1.25 Ga the continents Laurentia, Baltica, Ukraine, Amazonia, Australia and possibly Kalahari, Siberia and North China came together to form Hudsonland (also called Columbia and Nuna) [*Pesonen et*

al., 2003]. The occurrence of common features, geological belts and magmatic intrusions, along with paleomagnetic data support the hypothesis that subduction south of the Wyoming Craton may have subducted oceanic lithosphere - containing subduction related island arc terrains - that separated Laurentia from Australia [*Pesonen et al.*, 2003].

The location of synsubduction magmatism offshore in oceanic lithosphere south of the Wyoming Craton, rather than inboard or bordering the Wyoming Craton indicates that subduction was primarily south dipping. However, an anomalously high velocity region north of the Cheyenne Belt dipping to the north at 45° with an 80 km width [*Yuan and Dueker*, 2005] cannot be explained with simple south dipping subduction. It is called the Wyoming slab and at least two solutions have been proposed to explain this anomaly, both including a temporary cessation of south dipping subduction due to the accretion of two substantial island arc bodies called the Green Mountain Arc (GMA) and the Rawah Arc (RA). In the first solution south-dipping subduction brings the GMA into collision with the Wyoming Craton's southern margin. The force of the collision, and the buoyancy of the GMA, force remaining oceanic lithosphere north under the Wyoming Craton in a north dipping orientation producing the Cheyenne Slab [*Tyson et al.*, 2002]. In the second solution south-dipping subduction brings both the GMA and RA into collision with the Wyoming Craton, but north-dipping subduction occurs south of the RA. Subducted volatile related magmatism then produced a ~200 km wide back-arc basin between the GMA and RA. Under further subduction pressure the back-arc basin was subducted with a north dipping orientation producing the Cheyenne Slab [*Yuan and Dueker*, 2005].

Both solutions require a flip of the orientation of subduction, i.e. south dipping subduction switching to north dipping subduction. A modern analog for a flip in subduction orientation exists where the Banda arc and the Australian plate converge. [*Yuan and Dueker*, 2005].

The accretion of more subduction related island arc terrains followed the collision of the GMA and RA to the Wyoming Craton and placement of the Cheyenne Slab. Marine arc related sediments are found in regions of the Yavapai Province including ophiolites, pillow basalts and turbidites [*Whitmeyer and Karlstrom*, 2007]. Near the end of the formation of the Yavapai Province it was deformed by northwest – southeast shortening causing crustal thickening due to continued subduction of island arc terrains. Granitic plutons were formed in the western Yavapai as a result of north dipping subduction. Together these forces produced metamorphism related to burial depths of 10 – 20 km and large lateral temperature gradients [*Karlstrom and Williams*, 2006].

1.8 Figures

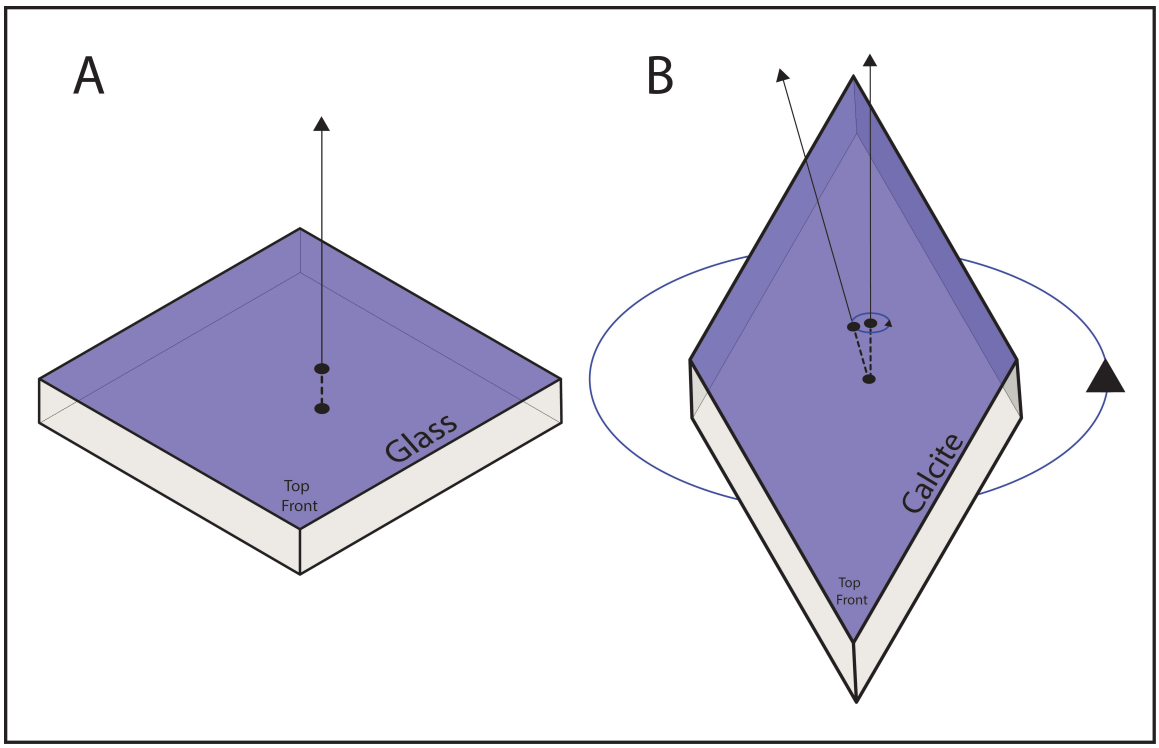

Figure 1.1. A demonstration of the effects of light travelling through isotropic and anisotropic material. Each material is placed on a piece of paper where a dot has been drawn. A. The isotropic material, in this case glass, transmits a single refraction of the dot regardless of how the glass is moved. B. When the same procedure is conducted with an anisotropic substance, like calcite, two refractions are produced by the material. The material has split the light into two separate orientations. As the calcite is rotated, one of the refracted circles will appear stationary as the other rotates around it. Measurements of the refracted light through calcite are dependent on the orientation of the material.

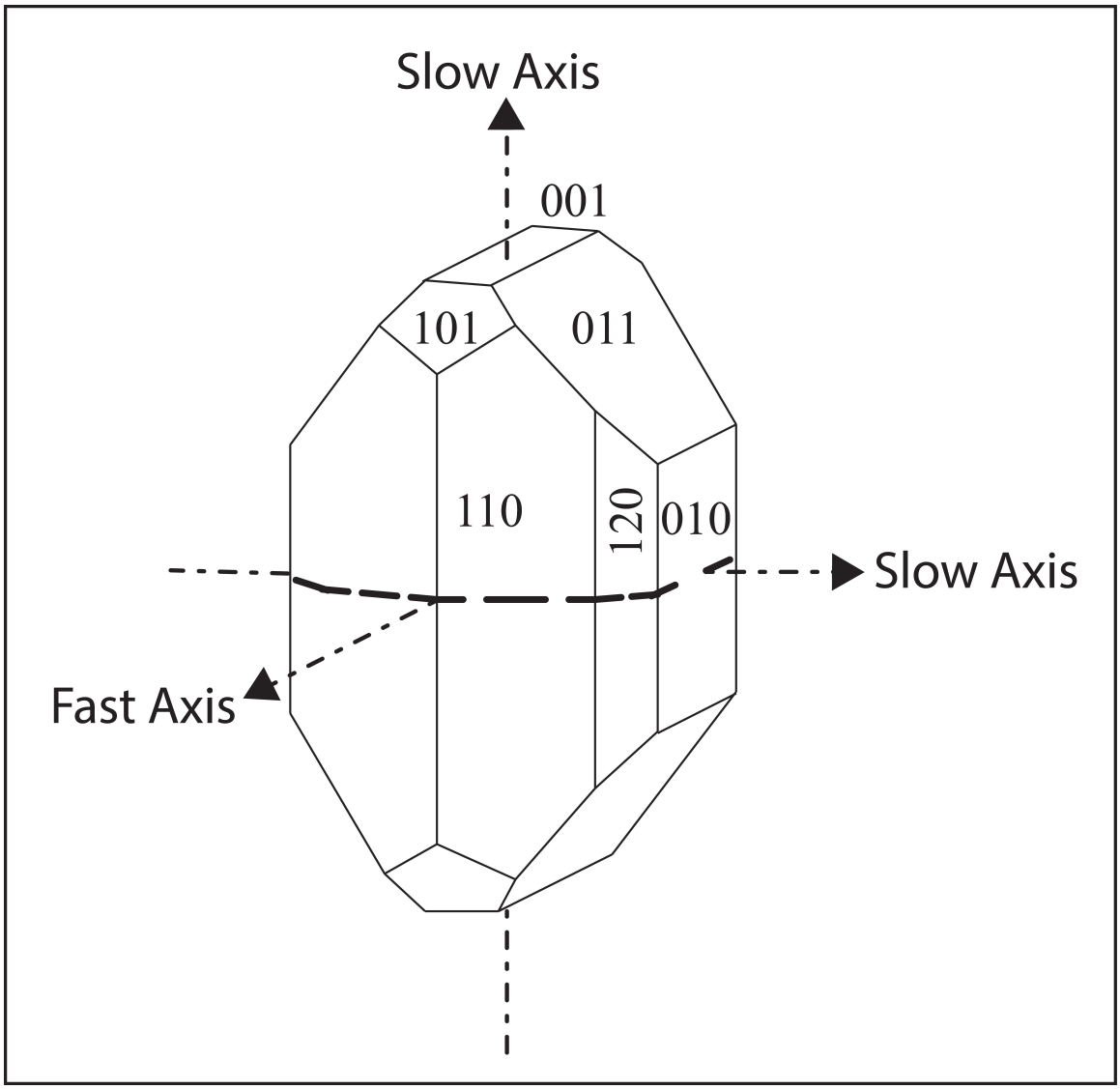

Figure 1.2. This is a crystallographic depiction of an olivine crystal. It has been shown that in most circumstances in the Earth's upper mantle that olivine crystals affected by a strain will become oriented so that the crystal's fast axis is parallel to the primary strain axis. After *Nesse* [2004].

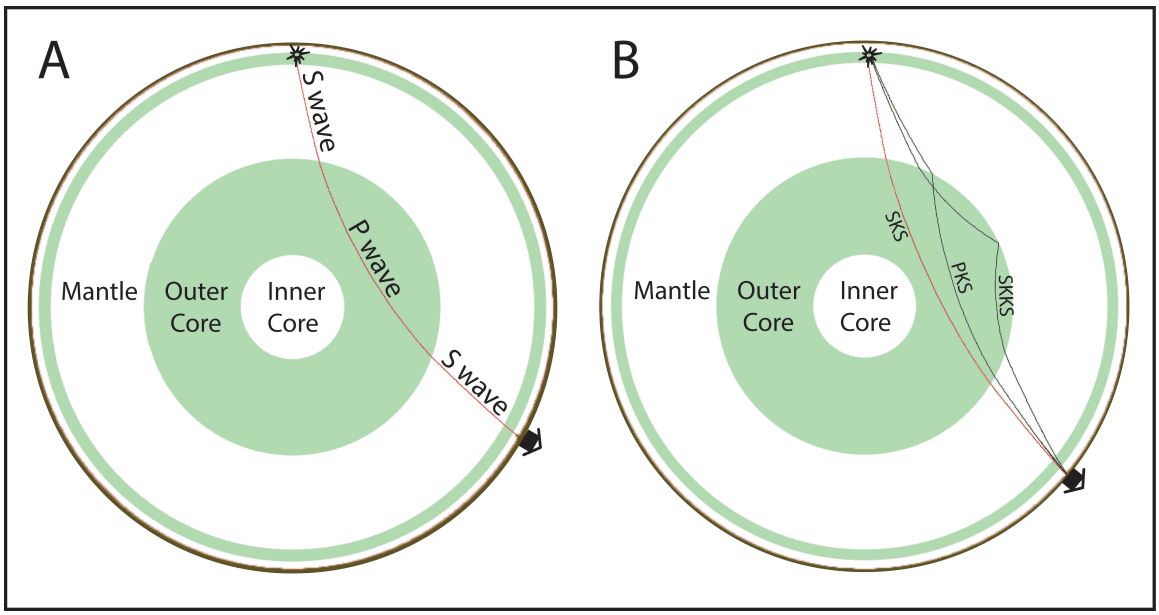

Figure 1.3. A. Depiction of an SKS wave. This wave begins as an S wave, but some of its energy is transferred to a P wave when it encounters the Earth's outer core. The outer core is liquid and does not support S wave particle motion. Any information about anisotropy the original S wave collected prior to its encounter with the outer core is lost when some of its energy becomes a P wave. When the P wave reaches the mantle, some of its energy becomes a new S wave. In this way, any anisotropy detected from an SKS wave is known to have occurred in the mantle between the outer core and the seismometer. B. Depiction of the phases used in this study: SKS, PKS, SKKS. After *Crotwell* [1999].

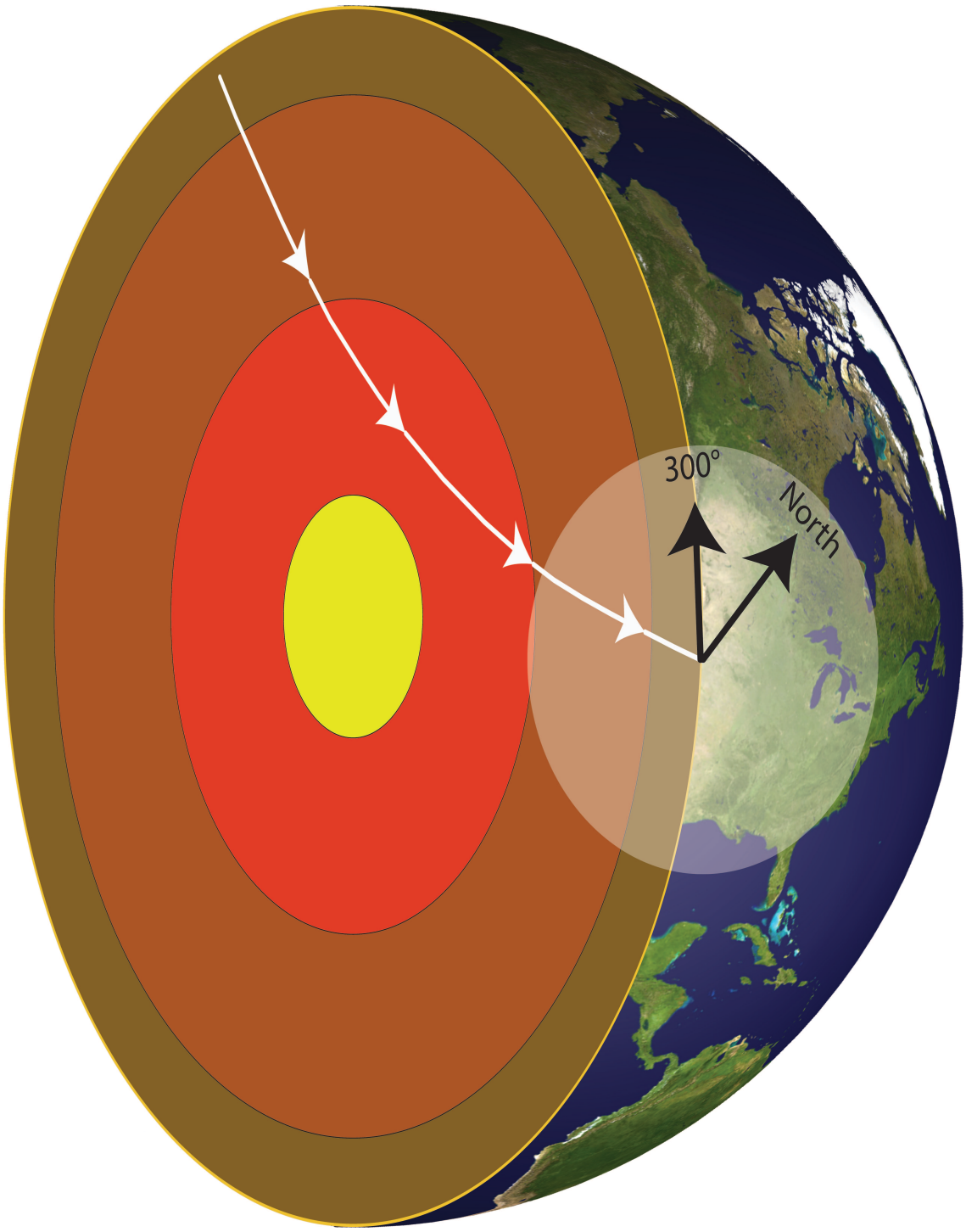

Figure 1.4. A seismic signal's back azimuth is defined as the azimuth from the seismometer to the epicenter of the source. White line depicts the path of an SKS phase as it travels through the earth. Back-azimuth arrow (300°) indicates the direction from the seismometer back to the earthquake epicenter.

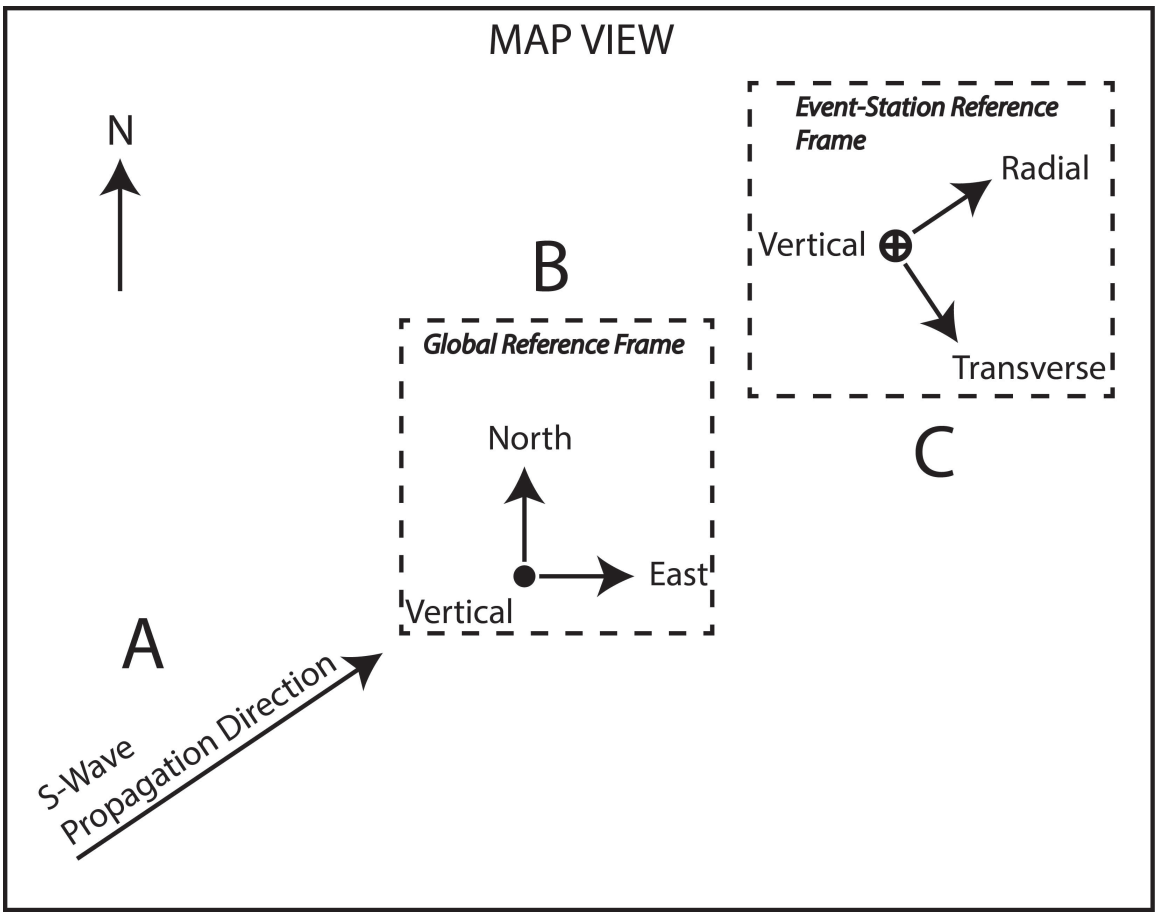

Figure 1.5. Seismic data orientation. A. The orientation of an incoming seismic signal. B. The seismometer records the signal using a global reference frame. C. Data is moved to an event-station reference frame for further processing.

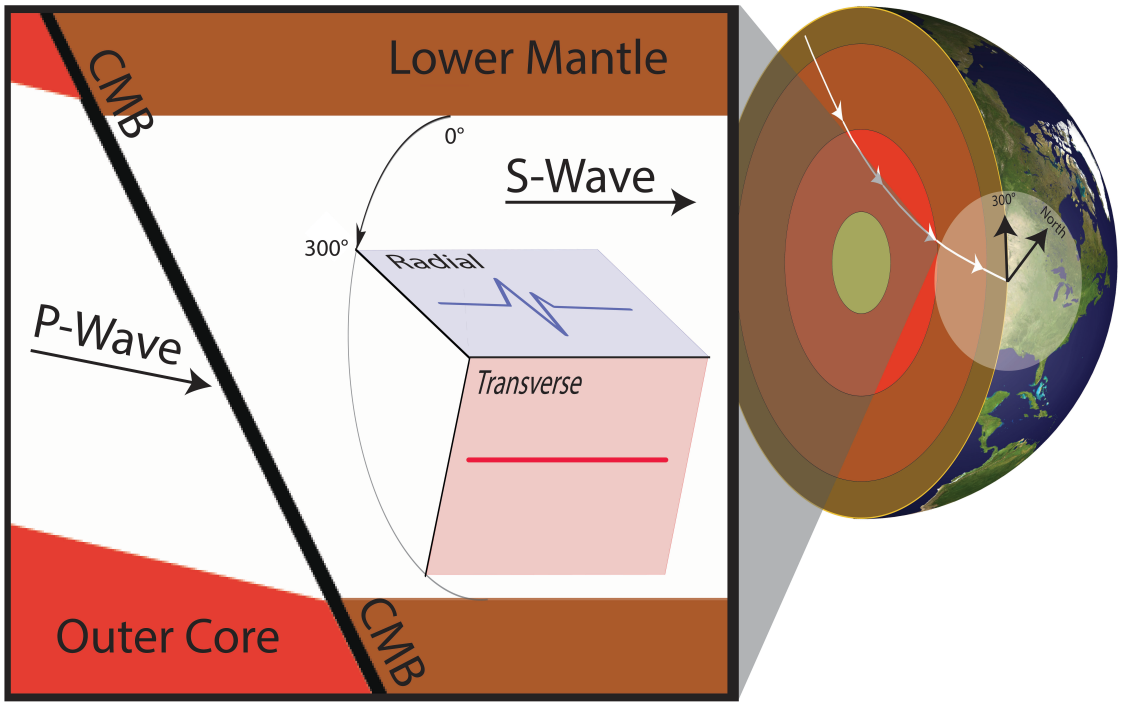

Figure 1.6. White regions represent the path of P wave and S wave propagation. As the P wave, approaching from a back-azimuth of 300° passes the CMB (core mantle boundary) some of its energy is converted into an S wave. All of the energy in this new S wave produces particle motion perpendicular to the wave's direction of propagation, and in the radial plane. The great circle path produced by the radial plane's intersection with the surface of the earth is oriented along the event-station back azimuth.

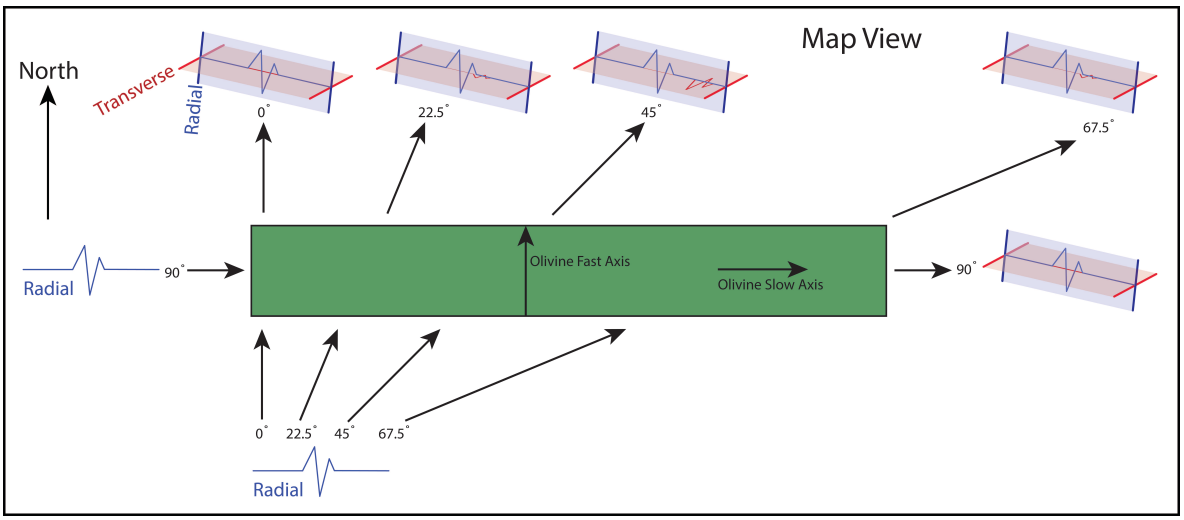

Figure 1.7. Depictions of effects of back azimuth on SKS splitting. Note: the fast axis of the anisotropy is 0°. For SKS waves approaching from back azimuths parallel and perpendicular to 0°, for example 0° and 90°, the transverse wave contains no energy—a result indistinguishable from the case with no anisotropy. The maximum transverse component energy is found for back azimuths midway between 0° and 90°, at 45°. From 0° to 45° the anisotropic effect on transverse energy increases, while from 45° to 90° the effect diminishes. This example uses only the first quadrant of the Cartesian plane. The same pattern occurs in the other three planes so that no anisotropic effect occurs when the SKS wave approaches from 0°, 90°, 180° and 270°, while the maximum effect occurs at 45°, 135°, 225° and 315°.

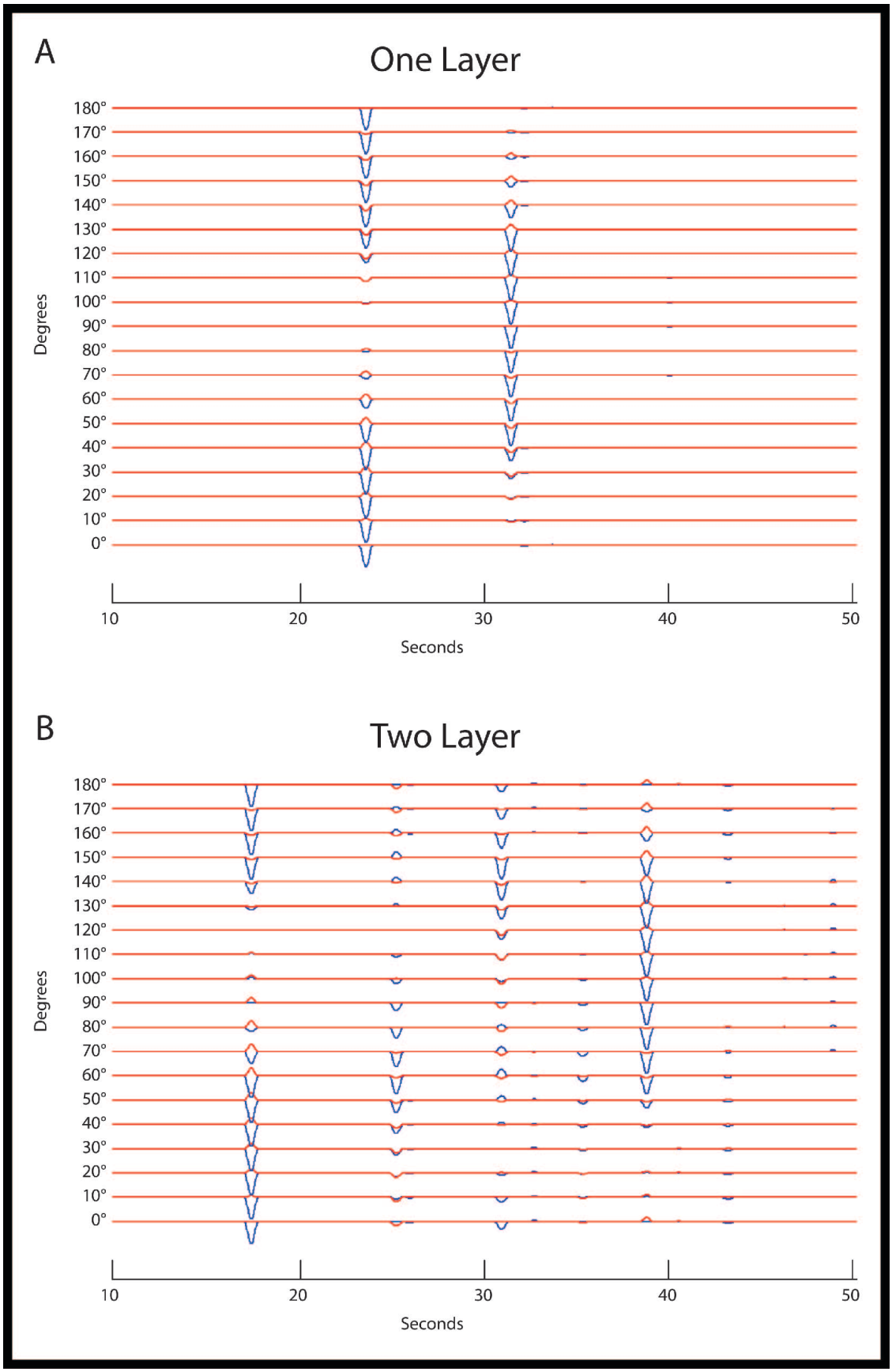
A
One Layer
180°
170°
160°
150°
140°
130°
120°
110°
100°
90°
80°
70°
60°
50°
40°
30°
20°
10°
0°
Degrees
10
20
30
40
50
Seconds
B
Two Layer
180°
170°
160°
150°
140°
130°
120°
110°
100°
90°
80°
70°
60°
50°
40°
30°
20°
10°
0°
Degrees
10
20
30
40
50
Seconds

Figure 1.8. Synthetic seismograms. These are highly simplified synthetic impulse response seismograms. Convolving these seismograms with a ricker wavelet and adding random noise can produce more realistic complexity. In both figures blue depicts radial energy, and red depicts transverse energy. The x-axis is an arbitrary time scale that is common to both figures. The y-axis is the back azimuth in degrees. A. Synthetic seismograms of *KS wave encountering a single layer of anisotropic material with a strike of 0° and a dip of 0°. Waves approaching from back azimuths of 0° and 180° incur no shear wave splitting. All energy traversed the material's fast axis and remains on the radial component (the pulses at ~ 23 s). Waves approaching from back azimuths of 90° and 270° (not shown) also incur no shear wave splitting, but all energy traversed the material's slow axis and remains on the transverse component (the pulses at ~ 32 s). Waves approaching from all other back azimuths incur varying degrees of shear wave splitting as their energy transits both the fast and slow axes. B. Synthetic seismograms of *KS wave encountering two layers of anisotropic material. Layer 1: strike of 0°, dip of 0°, Layer 2: strike 30°, dip of 0°. When the *KS wave encounters the lower layer of anisotropic material (Layer 2), splitting does not occur for back azimuths of 30°, 120°, 210° and 300°. Splitting does occur to a varying degree for all other back azimuths. Waves exit the lower layer, either split or not split, and enter the upper layer of anisotropic material (Layer 1). Here further splitting occurs for all waves not parallel to the upper layer's fast or slow axes.

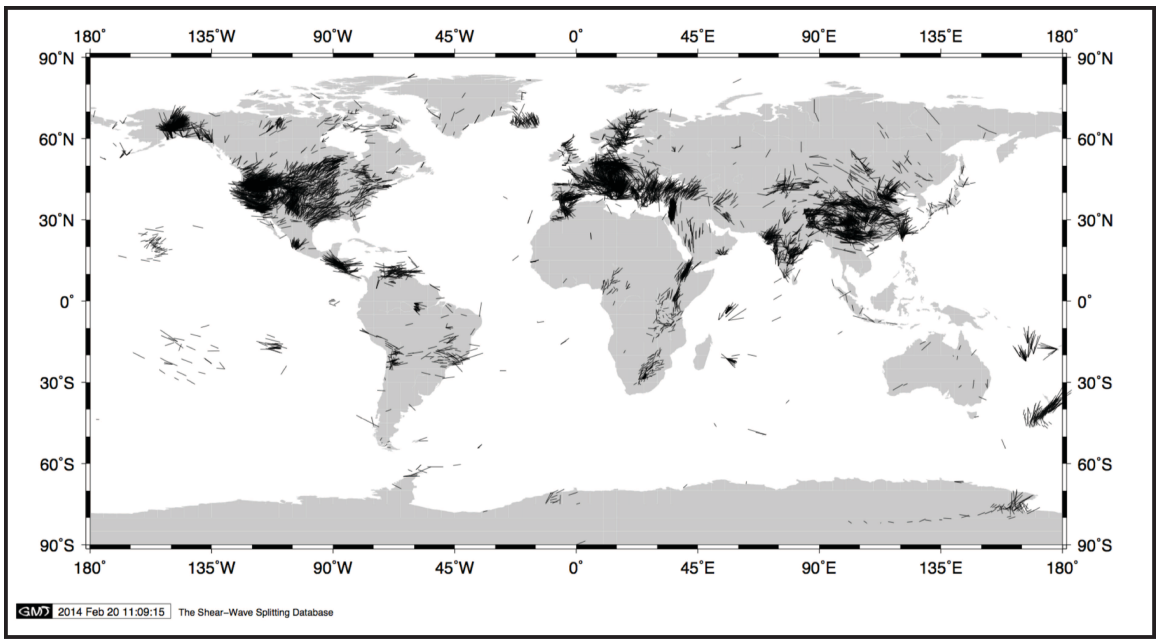

Figure 1.9. Map of some of the shear wave splitting results released in peer-reviewed journals. Each black line indicates a shear wave splitting result. The line orientation informs of the direction of anisotropy while the length of the line is related to the degree of anisotropy. [*Wüstefeld et al.*, 2009]

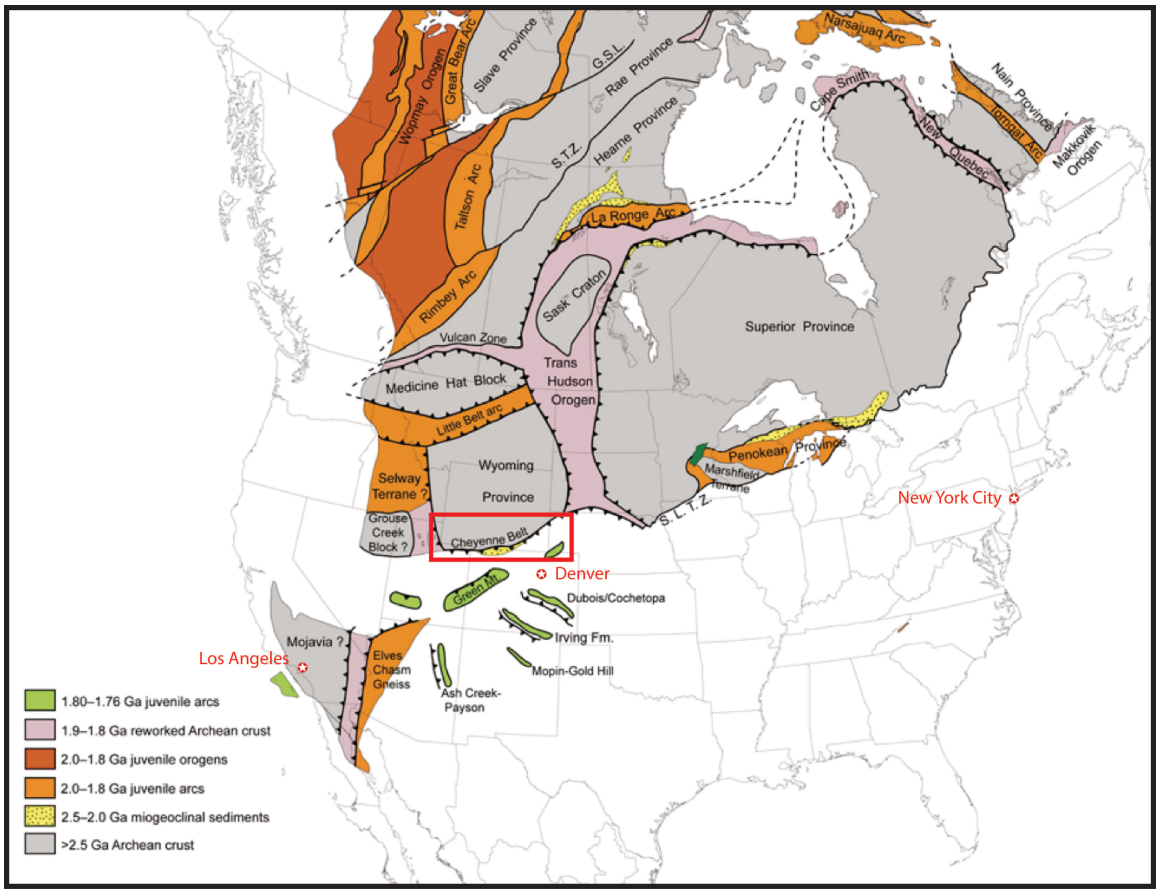

Figure 1.10. A depiction of the North American continent ~1.76 Ga. White stars in red circles note the locations of Los Angeles, CA, New York City, NY and Denver, CO for reference. Red box contains the southern edge of the ~2.5 Ga Wyoming Province which later became the northern side of the Cheyenne Belt. After *Whitmeyer and Karlstrom* [2007].

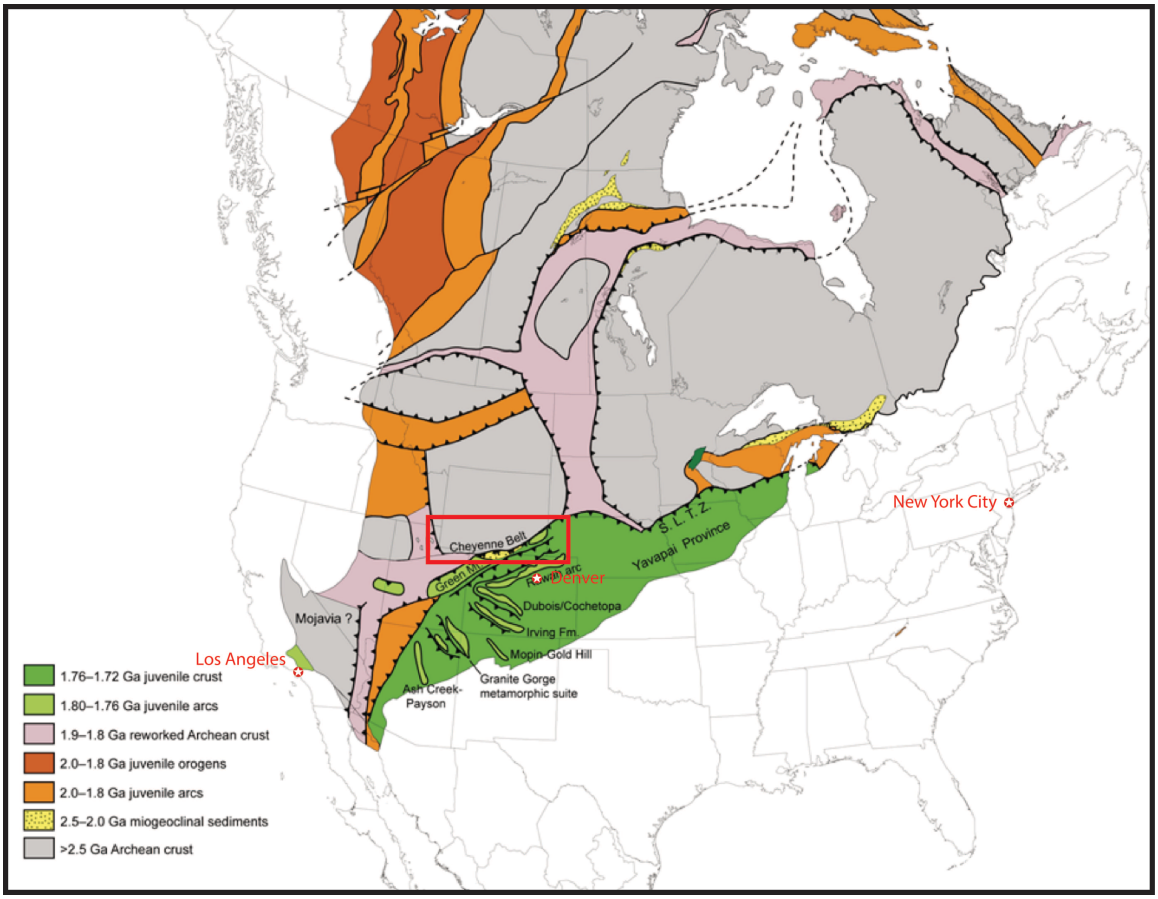

Figure 1.11. A depiction of the North American continent ~1.72 Ga. Local subduction moved island arcs toward the Wyoming Province where they accreted to the continent to form the southern side of the Cheyenne Belt, the Yavapai Province. After *Whitmeyer and Karlstrom* [2007].

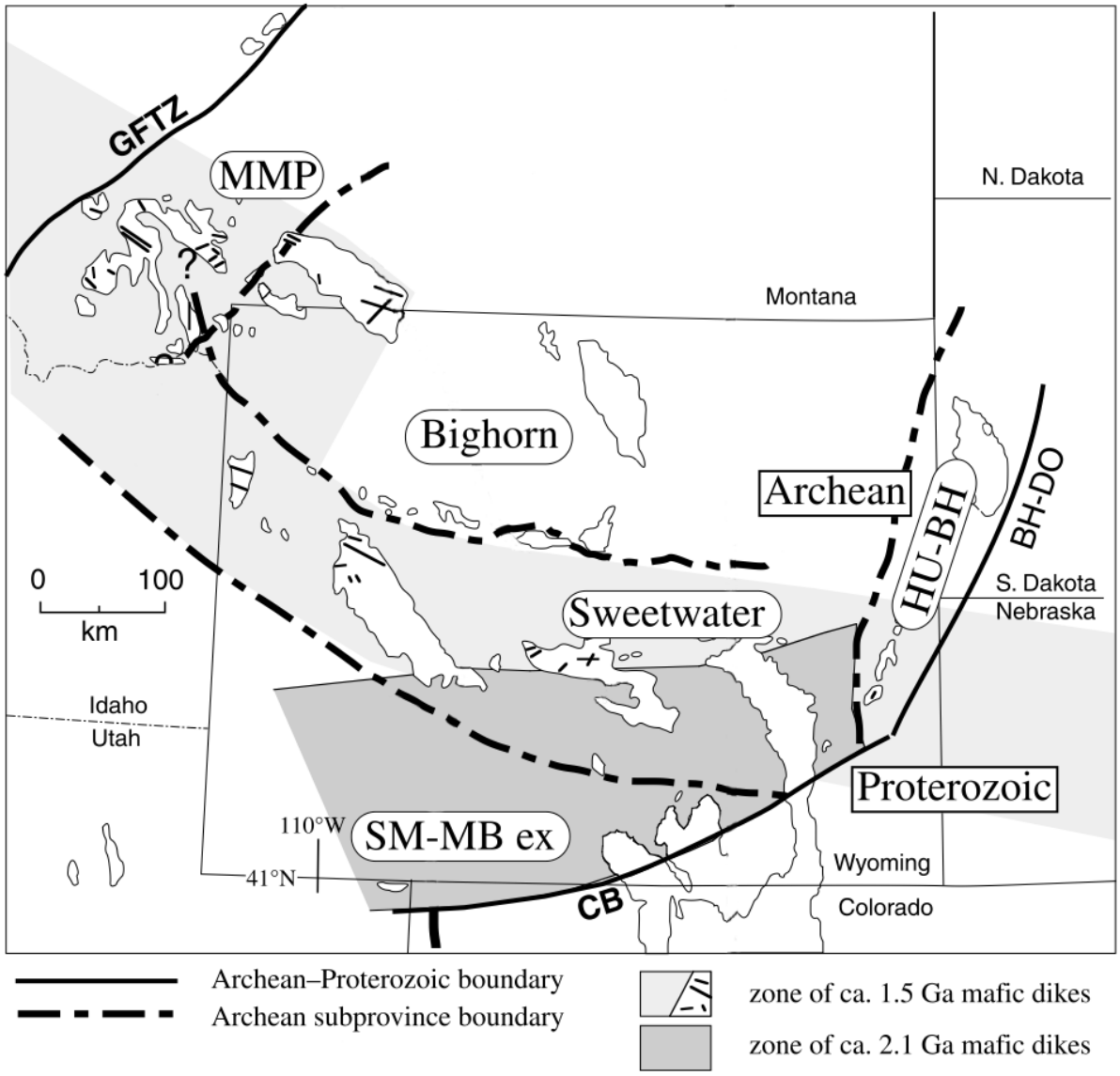

Figure 1.12. A depiction of the five sub-provinces of the Cheyenne Belt. MMP – Montana Metasedimentary Province; Bighorn – Bighorn Subprovince; Sweetwater – Sweetwater Subprovince; SM-MB – Sierra Madre Medicine Bow Exotic Block; HU-BH – Hartville Black Hills Block. After *Chamberlain et al.*[2003].

CHAPTER 2

INDICATIONS OF COMPLEX LITHOSPHERIC STRUCTURE AROUND THE CHEYENNE BELT IN THE WESTERN U.S. BASED ON SHEAR WAVE SPLITTING ANALYSIS

2.1 Introduction

The Cheyenne Belt is a major North American suture zone where Proterozoic island arc terrains were accreted onto the Archean Wyoming Province between 1.80 and 1.70 Ga [*Whitmeyer and Karlstrom*, 2007] (Fig. 2.1). In this study, the portion of the Cheyenne Belt in southeastern Wyoming was investigated. Here, the Cheyenne Belt bends from a north-northeast trajectory to a west-southwest trajectory.

North of the Cheyenne Belt the Wyoming Province underlies most of Wyoming and the adjacent states. South of the Cheyenne Belt the Yavapai Province underlies most of Colorado. The Cheyenne Belt remains a detectable, and in some places very complex, expression of southern lithospheric growth of Laurentia during the Proterozoic.

The seismic technique of shear wave splitting (SWS) exploits the anisotropic characteristic of certain minerals, primarily olivine, found in the earth's mantle. Research has determined that dislocation creep, thought to be the dominant deformation mechanism in the uppermost mantle, aligns olivine with its fast axis parallel to the maximum strain direction via a lattice preferred orientation (LPO) [*Long and Silver*, 2009] (Fig. 2.2). Core phases, particularly SKS, PKS and SKKS (hereafter called *KS) are useful because the effects of any event-side anisotropy are lost as some of the S wave energy is converted into P wave energy at the core-mantle boundary (CMB) (Fig. 2.3). When the P wave exits the outer core, some of its energy is converted to a

new radially polarized S wave with a known orientation dictated by the wave's back-azimuth, and initially no anisotropic effects. Once recorded by a seismometer, the *KS wave can be converted from the north, east and vertical reference frame used by the seismometer to the radial, transverse and vertical reference frame. In this orientation all *KS energy exiting the core will be on the radial channel. Energy found on the transverse channel indicates probable anisotropy between the core-mantle boundary (CMB) and the seismometer. Detected anisotropy is then considered to be the integrated effects of all anisotropic material the S wave encountered from CMB to seismometer. Measurements of shear wave splits (SWS) are often quantified with the parameters (ϕ) fast-axis orientation and (δt) delay time between fast axis and slow axis arrivals.

The in situ mantle below the continents is inaccessible to direct observation. Observations based on olivine anisotropy, detected through SWS, are one way to infer mantle flow characteristics and lithospheric fossil strain orientations. With these observations we hope to provide new constraints on the region surrounding the Cheyenne Belt that will improve our understanding of this Proterozoic suture zone.

2.2 Site Description

The Cheyenne Belt separates the Archean Wyoming Craton to the north from the Proterozoic Yavapai Province to the south. It is a Proterozoic suture zone expressed as a multi-fault, northeast striking, subvertical shear zone [*Sullivan and Beane*, 2013].

Rifting, possibly related to the breakup of Kenorland, along the southern margin of the Wyoming Craton occurred between 2.1 and 2.0 Ga forming a passive margin [*Pesonen et al.*, 2003], [*Chamberlain et al.*, 2003]. This passive margin accumulated ~300 Ma of sediments before its activation and closure [*Yuan and Dueker*, 2005].

Between 1.83 – 1.25 Ga the continents Laurentia, Baltica, Ukraine, Amazonia, Australia and possibly Kalahari, Siberia and North China came together to form the supercontinent Hudsonland (also called Columbia and Nuna) [*Pesonen et al.*, 2003]. The occurrence of common features, geological belts and magmatic intrusions, along with paleomagnetic data support the hypothesis that subduction south of the Wyoming Craton may have subducted oceanic lithosphere, containing subduction related island arc terrains, that separated Laurentia from Australia [*Pesonen et al.*, 2003].

The location of synsubduction magmatism offshore in oceanic lithosphere south of the Wyoming Craton, rather than inboard or bordering the Wyoming Craton indicates that subduction was primarily south dipping. However, an anomalously high velocity region north of the Cheyenne Belt dipping to the north at 45° with an 80 km width [*Yuan and Dueker*, 2005] cannot be explained with simple south dipping subduction. It is called the Wyoming slab and at least two solutions have been proposed to explain this anomaly, both including a temporary cessation of south dipping subduction due to the accretion of two substantial island arc bodies called the Green Mountain Arc (GMA) and the Rawah Arc (RA). In the first solution south-dipping subduction brings the GMA into collision with the Wyoming Craton's southern margin. The force of the collision, and the buoyancy of the GMA force remaining oceanic lithosphere north under the Wyoming Craton in a north dipping orientation producing the Cheyenne Slab [*Tyson et al.*, 2002]. In the second solution south-dipping subduction brings both the GMA and RA into collision with the Wyoming Craton, but north-dipping subduction occurs south of the RA. Magmatism related to subducted volatiles then produced a ~200 km wide back-arc basin between the GMA and RA. Under further subduction pressure the back-arc basin was subducted with a north dipping orientation producing the Cheyenne Slab [*Yuan and Dueker*, 2005].

Both solutions require a flip of the orientation of subduction, i.e. south dipping subduction switching to north dipping subduction. A modern analog for a flip in subduction orientation exists where the Banda arc and the Australian plate converge [*Yuan and Dueker*, 2005].

The accretion of more subduction related island arc terrains followed the collision of the GMA and RA to the Wyoming Craton and placement of the Cheyenne Slab. Marine arc related sediments are found in regions of the Yavapai Province including ophiolites, pillow basalts and turbidites [*Whitmeyer and Karlstrom*, 2007]. Near the end of formation the Yavapai Province was deformed by northwest – southeast shortening causing crustal thickening due to continued accretion of island arc terrains. Granitic plutons were formed in the western Yavapai as a result of north dipping subduction. Together these forces produced metamorphism related to burial depths of 10 – 20 km and large lateral temperature gradients [*Karlstrom and Williams*, 2006].

2.3 Data

Data used in this study came from broadband seismometers located between 39° and 42° north, and 105° and 109° W. This included the seismic arrays CD-ROM, Lodore, Laramie, CDROM, CREST and Earthscope transportable array stations, for a total of 235 sites. Using the Standing Order for Data (SOD) tool [*Owens et al.*, 2004], data for all SKS, SKKS, and PKS arrivals from M>5.8 earthquakes were reqested from the from the Incorporated Research Institutions for Seismology (IRIS) Data Management Center (DMC). Source distance ranges were 85-105°, 95-180°, and 125-150°, for the SKS, SKKS, and PKS, respectively.

2.4 Methods

Seismograms retrieved were visually inspected for a clear *KS arrival. An implementation of the [*Silver and Chan*, 1991] (SC) method for estimating the characteristics of seismic anisotropy was then applied. This method attempts to determine the combination of the

parameters δt and ϕ that best minimize transverse energy, thereby removing the effects of anisotropy. To accomplish this, a grid search is conducted over all reasonable pairings of δt and ϕ (δt values between 0 and 4 s; ϕ values between 0 and 180°) to find the most successful pair.

This implementation includes two modifications to the SC method. The first ensures that tangential energy is not over-corrected for by using a measurement of the pre-*KS tangential energy as the minimum corrected energy allowed. The second modification maps the corrected tangential splitting parameters into a probability density function for the identification a solution's confidence bounds.

Seismograms were then split into two groups based on the results of the SC method processing. Seismograms conforming to the following criteria were placed in Group (A):

- Signal to Noise Ratio > 2.5
- $\delta t < 3.0$ s
- δt error < 0.80 s
- ϕ error < 60.0°

Seismograms failing one or more of the criteria were placed in Group (B). Group (A) seismograms are considered the best data of this study. For this reason their splitting parameters were plotted without further processing. Group (B) seismograms, while not as good as those in Group (A), were still useful. They were combined with Group (A) seismograms, and stacked to improve signal to noise ratios and then plotted.

To stack the data, seismograms from stations were placed in two separate categories, depending on whether the stations were located north or south of the Cheyenne Belt. Then, the corrected transverse energy matrices from SC processing that define the transverse energy minimization for all combinations of δt and ϕ were summed using a Gaussian weight based on

distance from the station. For instance, for the 40 km stacks, a Gaussian distribution that becomes asymptotic with 0 at 40 km was used.. The degrees of freedom for each SC result were also stacked, and used with the stacked corrected tangential energy to calculate the stacked confidence bounds using the F-test [*Schutt et al.*, 1998; *Wolfe and Silver*, 1998]

2.5 Results

From the data collected, 136 stations produced good quality data. Of those, 29 produced the best data (Table 1). Similarly, 102 events were considered to be of good quality while 32 of those were considered the best events (Table 2). A total of 334 good quality signals were found with 55 of those considered the best signals (Table 3). Back azimuths for these 32 best signals were primarily from 240 - 330° (Fig. 2.4);

The final four seismic anisotropy result sets, Group(A), 0 km stacks, 40 km stacks and 100 km stacks are each quite different, and the plot for each will be analyzed separately.

2.5.1 Unstacked Group(A) Plot

Many of the splits in Group(A) (Fig. 2.5), both north and south of the CB are aligned sub-parallel to the direction of absolute plate motion (APM) [*Larson et al.*, 1997]. However, splits less than 200 km north of the CB have a variety of fast axis azimuths that vary considerably. Along the Laramie array splits and nulls appear orthogonal to APM.

2.5.2 0 km Stack Plot

The 0 km stacks plot (Fig. 2.6) contains fewer splits with fast axis azimuths similar to APM. Most that are sub-parallel to APM are again south of the CB. Within the Lodore array, large δt splits, approaching 4 s are both sub-parallel and orthogonal to APM. The region south of the CB contains a variety of spatially mixed azimuthal trends from Steamboat Springs to the

southern terminus of the study area, and splits along the Laramie array are orthogonal to APM.

2.5.3 40 km Stack Plot

In the plot of the 40 km stacks (Fig. 2.7) new trends emerge as stacks along the Deep Probe array show fast axis azimuths from 10 - 25° from north. This azimuth range is shared with stations in the Laramie array. Stations in the CDROM array show fast axis azimuths approaching 40° from north both above and below the CB. The region south of Steamboat Springs contains a mix of azimuths similar to those seen in the 0 km stacks, but now intermingled with stations from the CREST array showing azimuths similar to those of the Deep Probe array.

2.5.4 100 km Stack Plot

The plot of 100 km stacks (Fig. 2.8) continues with the shift towards north seen in the 40 km stacks plot throughout the Lodore and Deep Probe arrays with azimuths in the 5 - 15° range. Azimuths for stations in the CREST and CDROM arrays range from 10 - 20° from north.

The trend among the three plots of stacked splits appears to be one of sinistral rotation of fast axis azimuths from the 0 km plot to the 100 km plot. Both the 0 km and 40 km plots show multiple trends of fast axis orientation in the region south of Steamboat Springs. Stations with azimuths sub-parallel to APM are more common south of the CB.

2.6 Discussion

Differences among the seismic stations represented on each plot have occurred due to high error values inherent in some of the stacks.

2.6.1 Unstacked Group(A) Plot

Below the CB, except for stations in the Laramie array, the fast axis orientation (FAO) for most of the data is consistent with APM. This indicates that for these stations the anisotropy detected might be due to flow in the upper mantle. Unfortunately, the APM trend is very similar to the strike of the CB and the Proterozoic subduction, so this data could also represent fossil trench parallel anisotropy from the Proterozoic. Split, and null split data along the Laramie array are possibly the result of fossil trench perpendicular anisotropy from the Proterozoic. The variety of FAO detected above the CB in the Rawlins region indicate complex anisotropy due to either lateral heterogeneity or possible detection of two layers of anisotropic material.

2.6.2 0 km Stack Plot

Results in the region where the CB is poorly defined, between the brown dashed lines, the complex anisotropy could indicate both trench parallel and trench perpendicular anisotropy. Or trench parallel and APM anisotropy. The detection of two trends of FAO south of Steamboat Springs that are not consistent with APM could indicate the imbrication of fossil anisotropy due to deformation affecting the upper mantle.

2.6.3 40 km Stack Plot

At this level of stacking, new trends in the data appear. Data following a new trend with FAO of 5 - 15° is mostly found in the lower elevations of the study area as indicated by the lighter topographical shading in figure 2.7. Anisotropy with this FAO is interpreted to be fossil anisotropy from the Proterozoic collision event that produced the Yavapai Province and the Cheyenne Belt Suture Zone. Detected anisotropy beneath the higher elevations appears sub-parallel to APM.

When overlaid on a map of Pn velocity perturbations varying from an average Pn velocity of 7.95 km/s [*Buehler and Shearer*, 2012], relationships appear (Fig. 2.9). The higher elevation locations with sub-parallel to APM FAO coincide with average to 3% below average velocity perturbations indicating higher lithospheric temperatures. Lower elevation locations with fossil Proterozoic anisotropic fabric coincide with average to 3% above average velocity perturbations correlating to cooler lithosphere.

The interpretation of this finding is that north trending (5° - 15°) FAO lithospheric fabric formed throughout the region during the Proterozoic suturing event. It remained preserved until the Farallon plate sank into the asthenosphere ~20 Ma (Fig. 2.10). This event allowed hot asthenosphere to heat the lithosphere, lifting the modern Rocky Mountains via buoyancy and thermal expansion. Increased temperature also caused the local erasure of the Proterozoic fossil anisotropy.

While the FAO beneath the mountainous regions of the study area could be due to later fossil anisotropy in the lithosphere, it is more likely the result of regional mantle flow.

2.6.4 100 km Stack Plot

At the largest radius of stacking in this study, the dominant data trend of an FAO 5 - 25° from north is consistent with many of the null-split data. This is possibly an expression of the Proterozoic subduction stress field, fossilized and detectable in the present. However, low δt values may indicate that the 100 km stacking radius surpassed the data's statistical usefulness.

2.7 Conclusions

The modified *Silver and Chan* [1991] method for characterization of upper mantle seismic anisotropy has proven effective in constraining seismic anisotropy in the Cheyenne Belt region.

A previously undetected regional fossil fabric of north trending fast axis orientations in the topographically lower areas of the study site are interpreted as anisotropic remnants of the Proterozoic stress field from the accretion of the Yavapai Province to the Wyoming Craton. Regions of FAO sub-parallel to APM in the mountainous areas is due to post Farallon plate heating of the lithosphere that locally erased the Proterozoic fossil anisotropy.

2.8 Figures

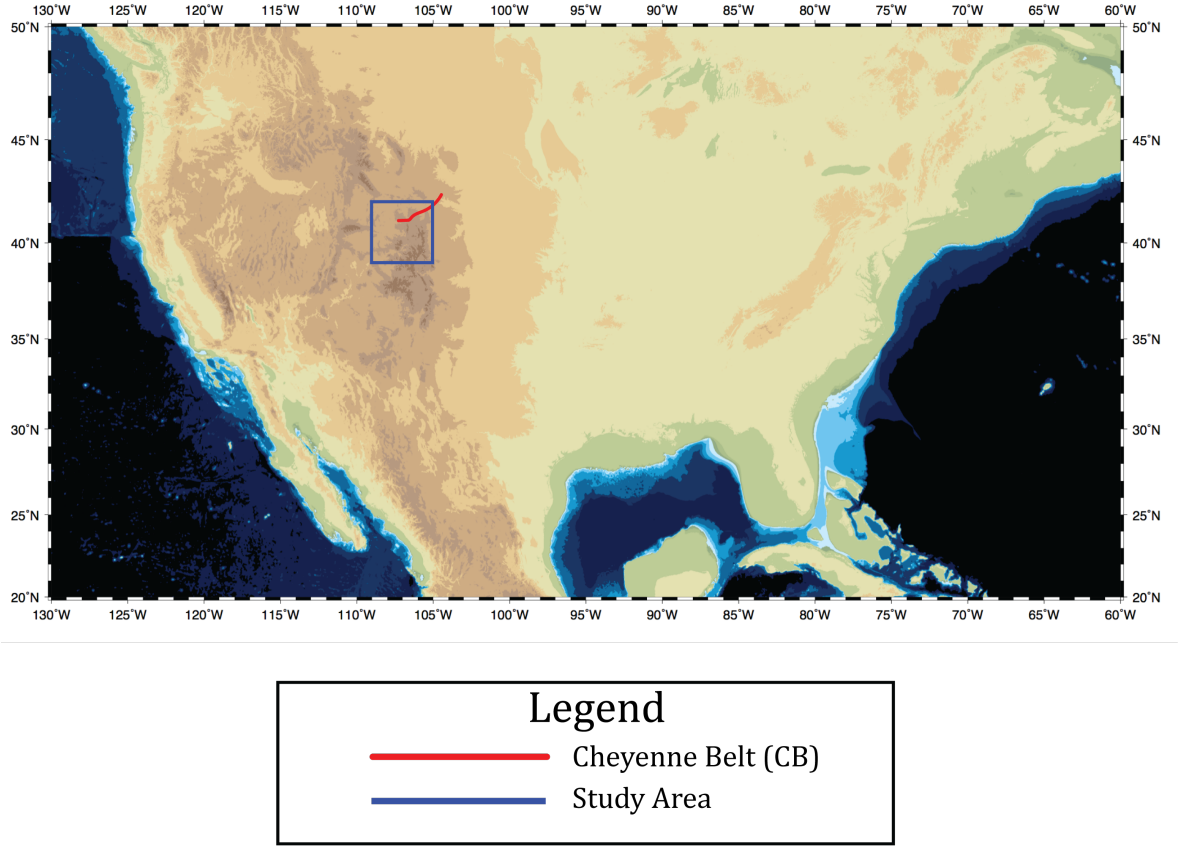

Figure 2.1 Map of North America with the Cheyenne Belt and the area of study highlighted.

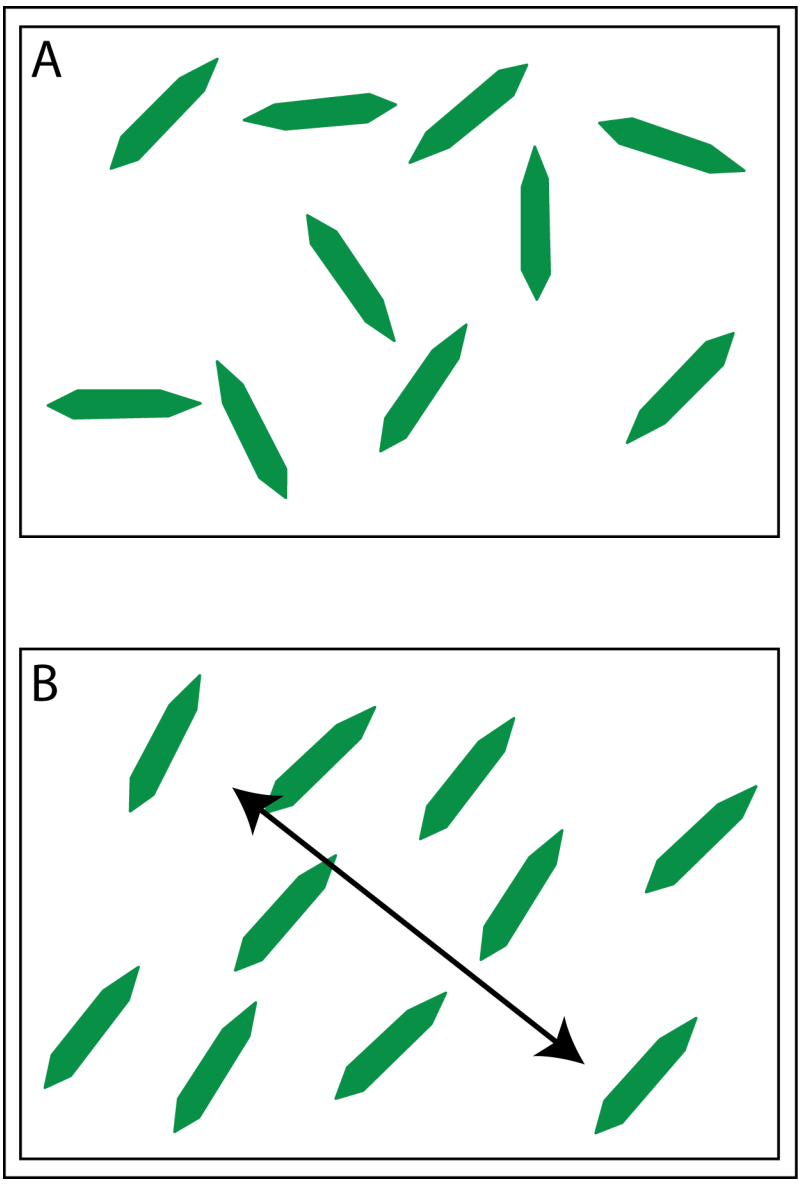

Figure 2.2. A depiction of the behavior of olivine crystals A. unstrained - no preferred orientation is observed; and B. strained - the crystalline structure of the olivine is altered via dislocation creep producing a lattice preferred orientation and anisotropy.

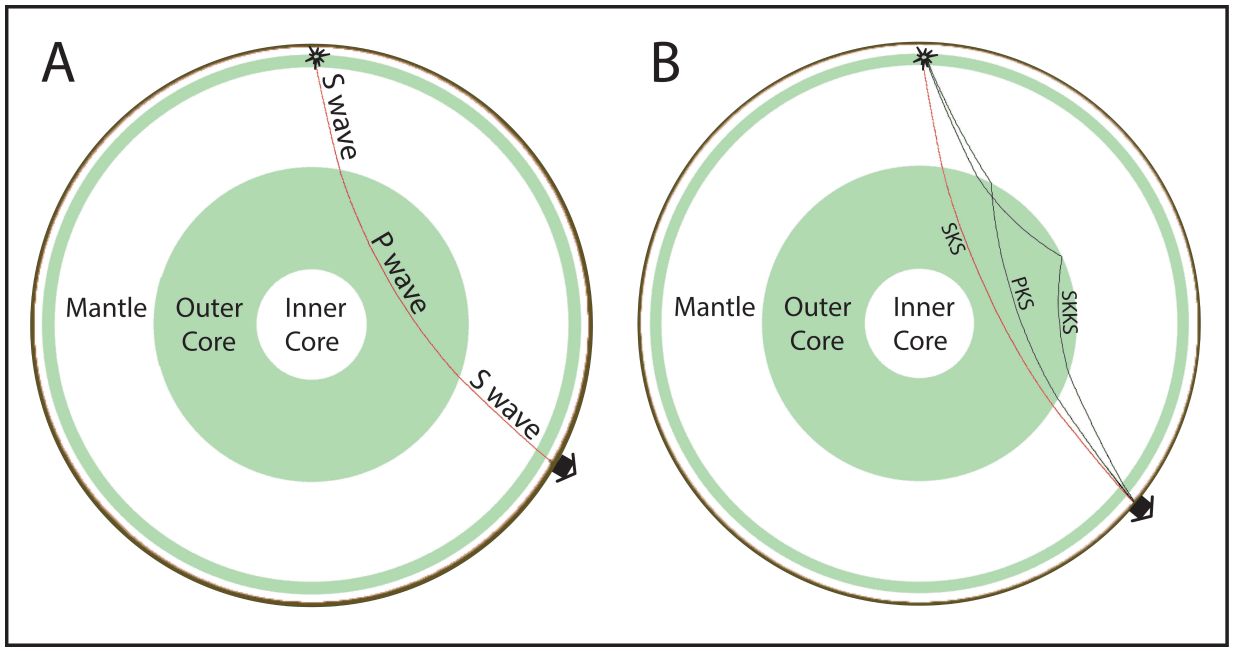

Figure 2.3. A. Depiction of an SKS wave. This wave begins as an S wave, but some of its energy is transferred to a P wave when it encounters the Earth's outer core. The outer core is liquid and does not support S wave particle motion. Any information about anisotropy the original S wave collected prior to its encounter with the outer core is lost when some of its energy becomes a P wave. When the P wave reaches the mantle, some of its energy becomes a new S wave. In this way, any anisotropy detected from an SKS wave is known to have occurred in the mantle between the outer core and the seismometer. B. Depiction of the phases used in this study: SKS, PKS, SKKS. After *Crotwell* [1999].

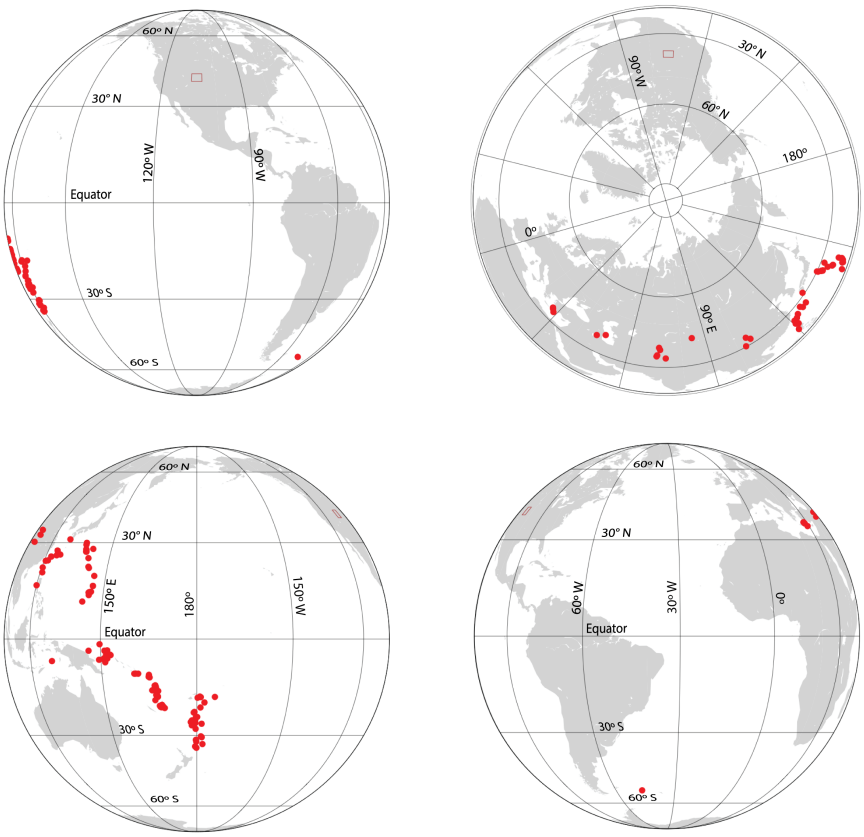

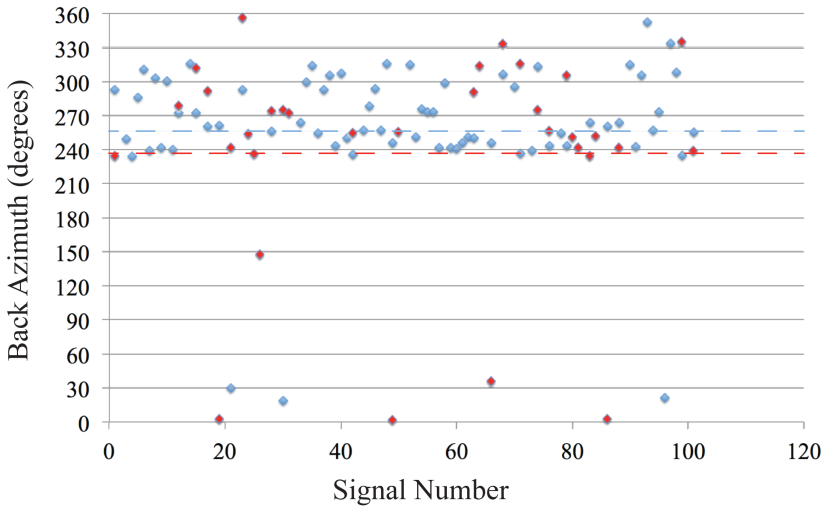

Figure 2.4. Upper for global projections depict the study site (red square) and earthquakes that provided data for the study. Lower plot shows back azimuth directions for Group(B) data in blue and Group(A) data in red. Blue and red dashed lines indicate the mean of Group(B) and Group(A) back azimuths respectively.

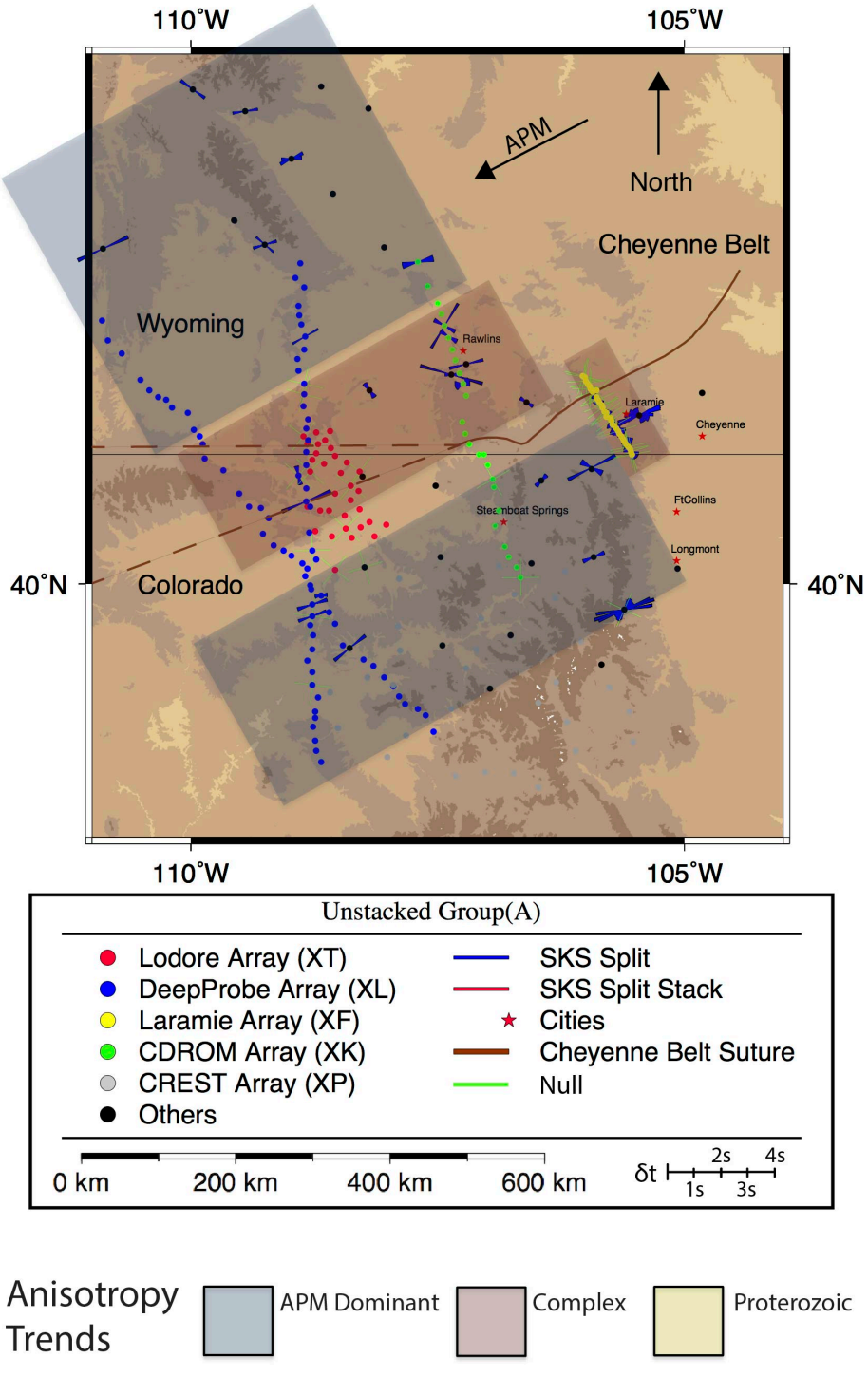

Figure 2.5. Plot of unstacked, Group(A) results. "Bowtie" symbols represent individual split measurements. The length of one side of bowtie represents the δt measurement. Width of bowtie represents the ϕ error in degrees.

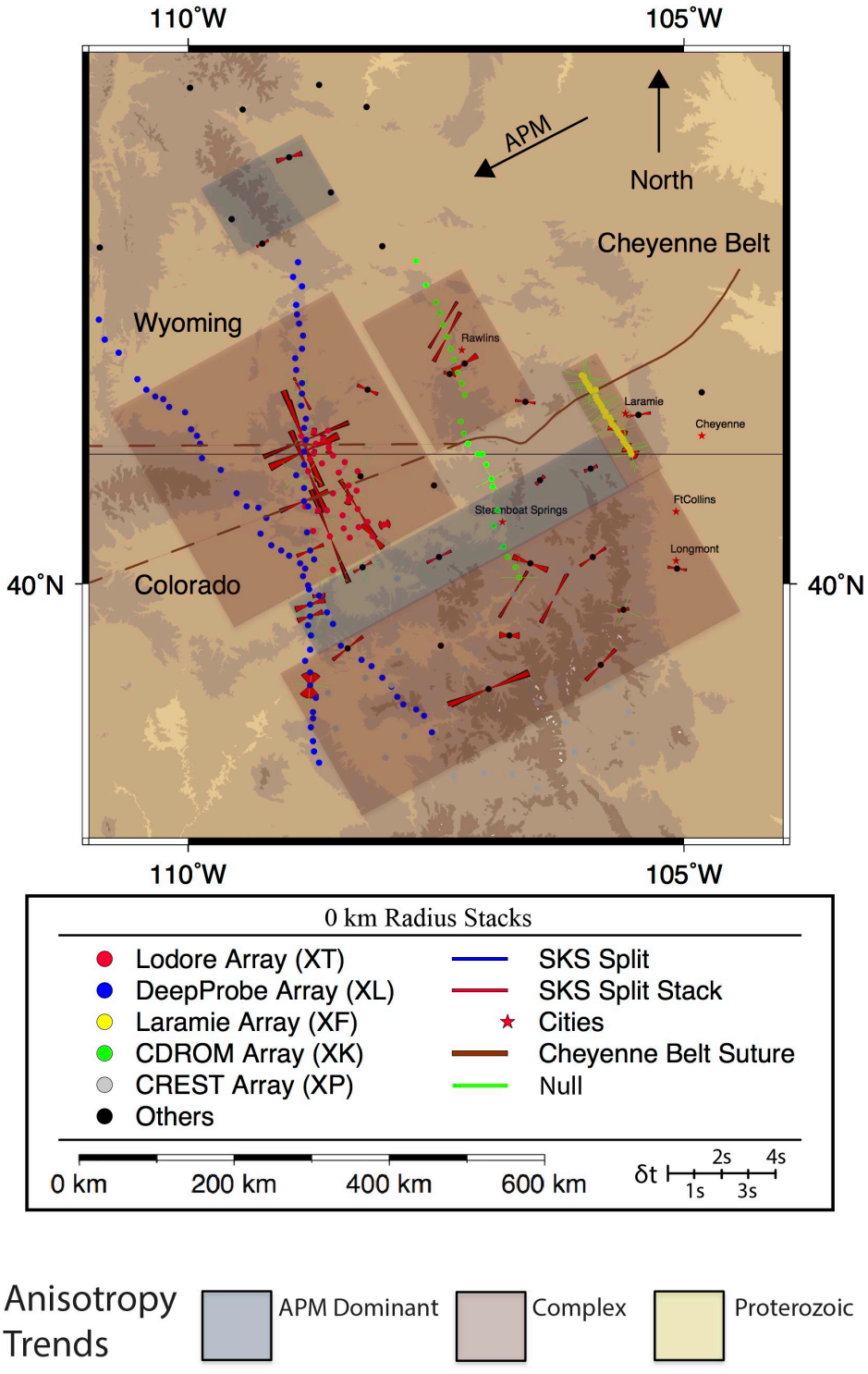

Figure 2.6. Plot of 0 km radius stack results. "Bowtie" symbols represent individual split measurements. The length of one side of bowtie represents the δt measurement. Width of bowtie represents the ϕ error in degrees.

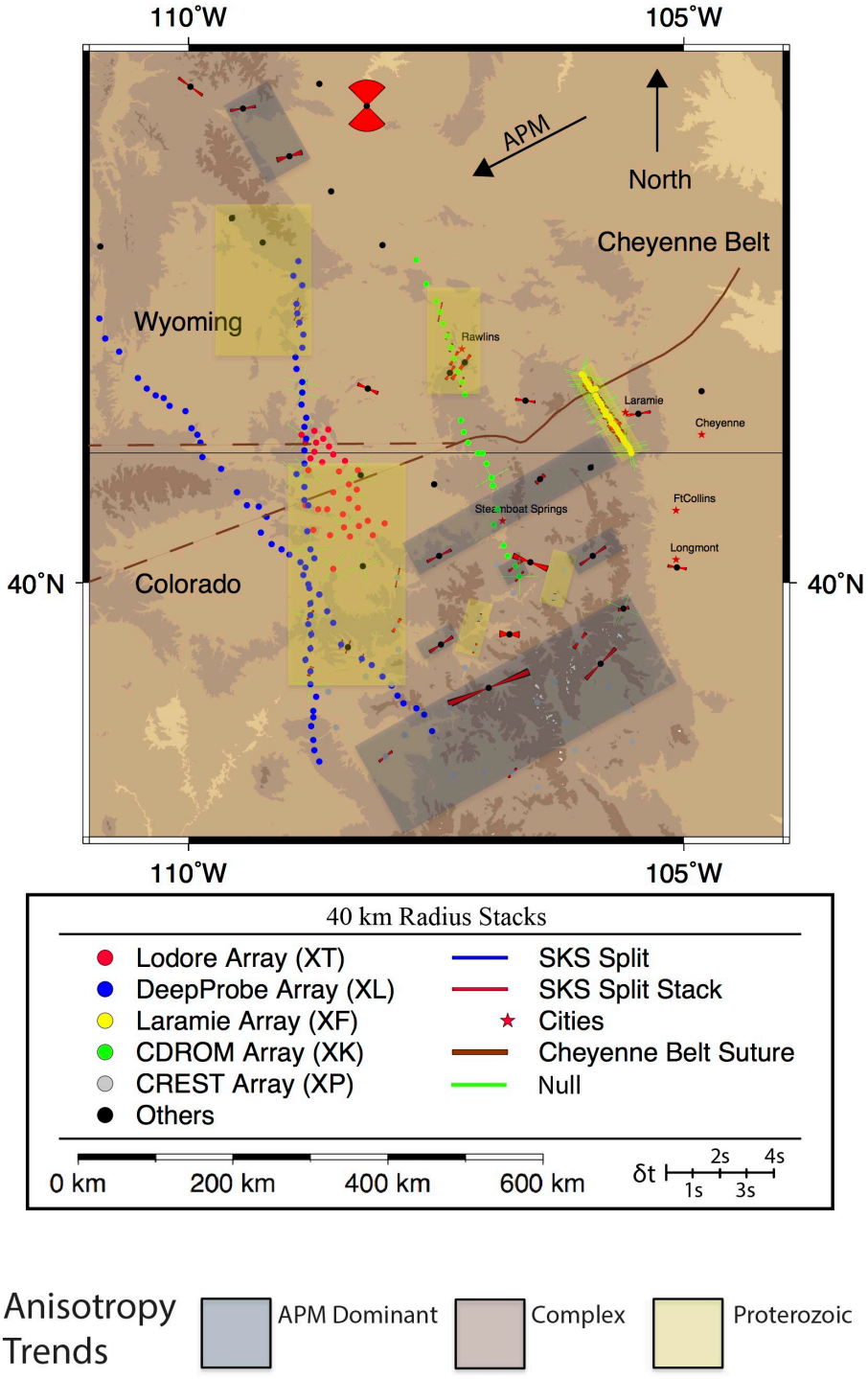

Figure 2.7 Plot of 40 km radius stack results. "Bowtie" symbols represent individual split measurements. The length of one side of bowtie represents the δt measurement. Width of bowtie represents the ϕ error in degrees.

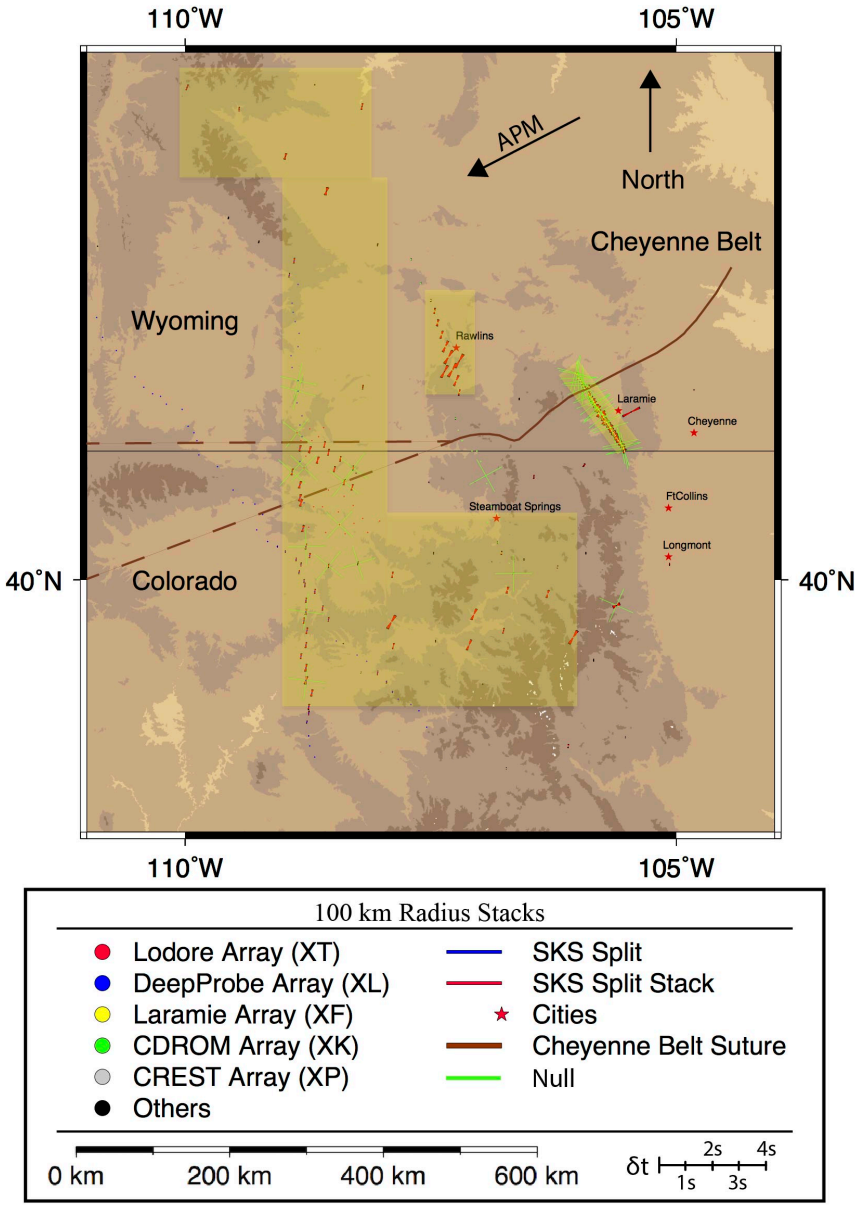

Figure 2.8. Plot of 100 km radius stack results. "Bowtie" symbols represent individual split measurements. The length of one side of bowtie represents the δt measurement. Width of bowtie represents the ϕ error in degrees.

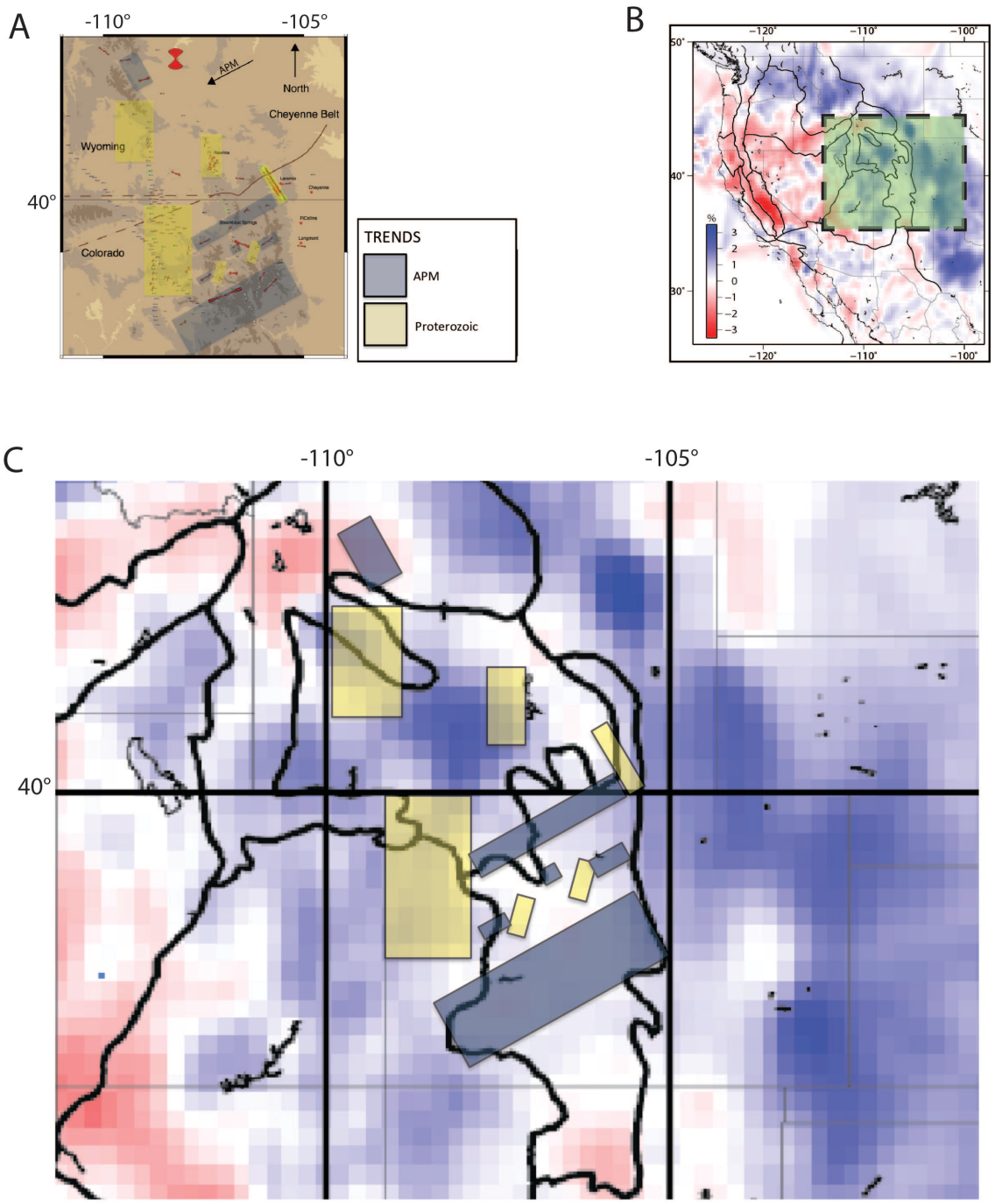

Figure 2.9. A. Results of the 40 km radius stacking from Figure 2.7. B. Plot of Pn velocity variations from *Buehler and Shearer*, [2012]. Region of study is highlighted in green. C. Regions of Proterozoic and APM trends from 40 km radius stacking overlain on a plot of Pn velocity variations. Regions of APM FAO correspond to average to hot lithosphere. Regions of Proterozoic FAO correspond to average to cold lithosphere.

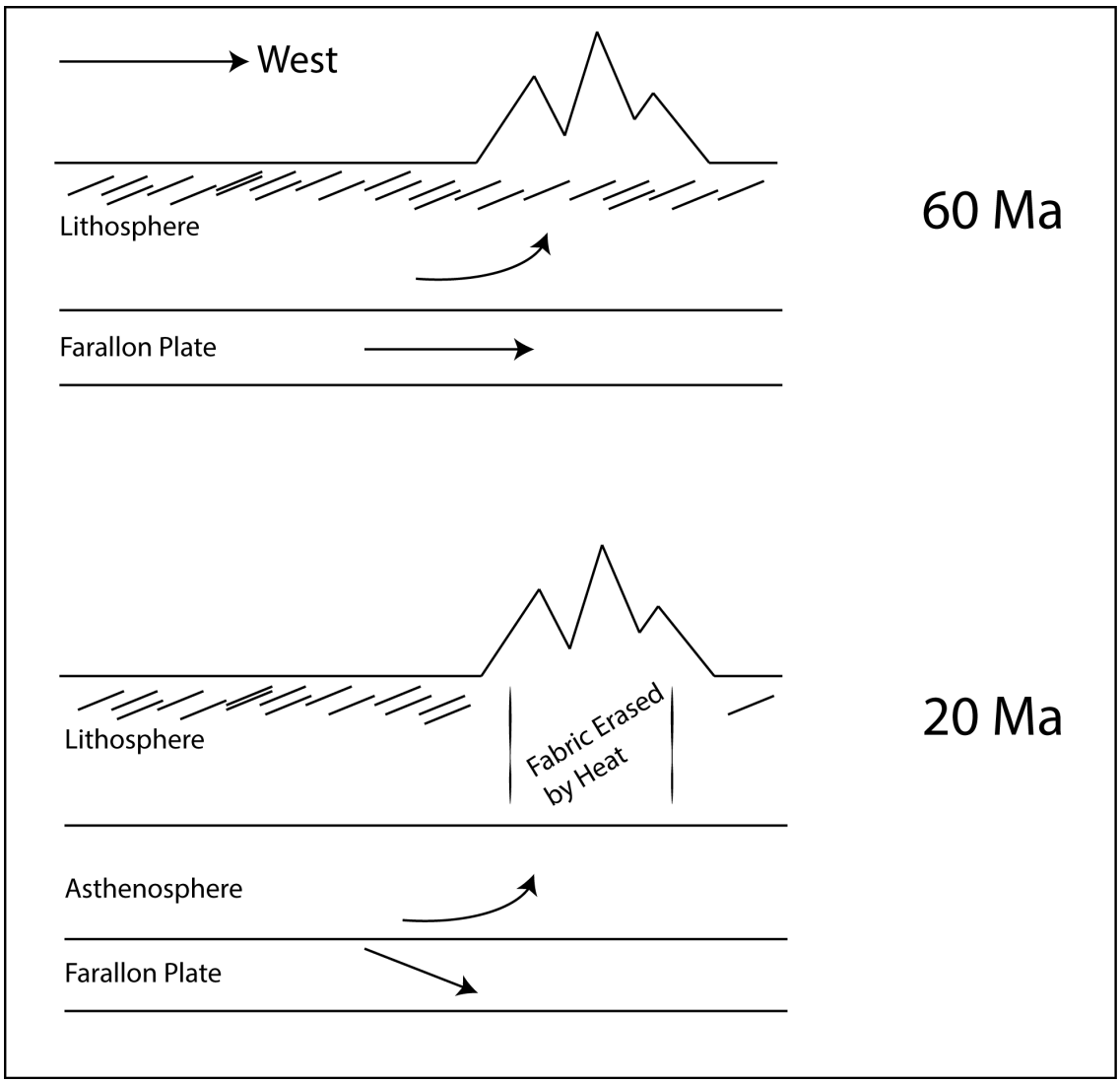

Figure 2.10. 60 Ma the Farallon plate forced the Laramide Orogeny. By 20 Ma hot asthenosphere contacting the lithosphere as the Farallon plate sank produced uplift and erasure of Proterozoic anisotropic fabrics locally.

2.9 Tables

Table 1. List of stations with data used in the study. Complete list comprises stations used for Group(B) data. Stations with an * in the "Best" column were also used for Group(A) data.

Best	Array	Station	Latitude	Longitude	Elevation (m)	Start Date	End Date	Instrumentation
	Lodore	CSD	40.44	-108.28	1931	1997/08/01	1998/07/15	sts2_vel:RT72A-08
	Lodore	DRY	40.70	-108.54	2059	1997/08/01	1998/07/15	sts2_vel:RT72A-08
	Lodore	JWM	40.57	-108.60	2077	1997/08/01	1998/07/15	sts2_vel:RT72A-08
	Lodore	LSC	40.53	-108.44	1802	1997/08/01	1998/07/15	sts2_vel:RT72A-08
	Lodore	NDH	40.37	-108.14	1957	1997/08/01	1998/07/15	sts2_vel:RT72A-08
	Lodore	PMR	41.08	-108.82	2164	1997/08/01	1998/07/15	sts2_vel:RT72A-08
	Lodore	POW	40.94	-108.42	2169	1997/08/01	1998/07/15	sts2_vel:RT72A-08
	Lodore	RRE	41.17	-108.73	2353	1997/08/01	1998/07/15	sts2_vel:RT72A-08
	Lodore	RRW	41.14	-108.86	2320	1997/08/01	1998/07/15	sts2_vel:RT72A-08
	Lodore	SMR	40.72	-108.30	1900	1997/08/01	1998/07/15	sts2_vel:RT72A-08
	Lodore	SWB	40.65	-108.38	1815	1997/08/01	1998/07/15	sts2_vel:RT72A-08
	Lodore	BLUE	40.99	-108.54	2098	1997/08/01	1998/07/15	sts2_vel:RT72A-08
	Lodore	CALA	40.11	-108.54	2345	1997/08/01	1998/07/15	sts2_vel:RT72A-08
	Lodore	CALI	40.37	-108.57	2085	1997/08/01	1998/07/15	sts2_vel:RT72A-08
	Lodore	DOUG	40.57	-108.69	2153	1997/08/01	1998/07/15	sts2_vel:RT72A-08
	Lodore	FWGP	40.96	-108.77	2077	1997/08/01	1998/07/15	sts2_vel:RT72A-08
	Lodore	GRAN	41.11	-108.64	2164	1997/08/01	1998/07/15	sts2_vel:RT72A-08
	Lodore	HELL	41.05	-108.58	2153	1997/08/01	1998/07/15	sts2_vel:RT72A-08
	Lodore	HIAW	41.01	-108.73	2105	1997/08/01	1998/07/15	sts2_vel:RT72A-08
	Lodore	JNMT	40.46	-108.02	2231	1997/08/01	1998/07/15	sts2_vel:RT72A-08
	Lodore	KINN	41.18	-108.59	2292	1997/08/01	1998/07/15	sts2_vel:RT72A-08
	Lodore	LANG	40.87	-108.29	2258	1997/08/01	1998/07/15	sts2_vel:RT72A-08
	Lodore	LIME	40.87	-108.79	2371	1997/08/01	1998/07/15	sts2_vel:RT72A-08
	Lodore	LOOK	40.86	-108.48	2415	1997/08/01	1998/07/15	sts2_vel:RT72A-08
	Lodore	MAYB	40.48	-108.19	1888	1997/08/01	1998/07/15	sts2_vel:RT72A-08
	Lodore	PINR	40.36	-108.37	2097	1997/08/01	1998/07/15	sts2_vel:RT72A-08
	Lodore	SUTT	40.58	-108.29	1852	1997/08/01	1998/07/15	sts2_vel:RT72A-08
	Lodore	TANK	40.41	-108.74	2441	1997/08/01	1998/07/15	sts2_vel:RT72A-08
	Lodore	TWIN	40.76	-108.38	1883	1997/08/01	1998/07/15	sts2_vel:RT72A-08
	Lodore	VMCK	41.08	-108.71	2136	1997/08/01	1998/07/15	sts2_vel:RT72A-08
	Lodore	YSCF	40.43	-108.43	1966	1997/08/01	1998/07/15	sts2_vel:RT72A-08
	Lodore	ZENO	40.60	-108.82	2302	1997/08/01	1998/07/15	sts2_vel:RT72A-08
	Laramie	L01	41.00	-105.53	8160	2000/09/01	2001/12/31	sts2_vel:RT72A-08
*	Laramie	L02	41.02	-105.54	1.8	2000/09/01	2001/12/31	sts2_vel:RT72A-08
	Laramie	L03	41.04	-105.55	8050	2000/09/01	2001/12/31	sts2_vel:RT72A-08
	Laramie	L04	41.06	-105.57	7970	2000/09/01	2001/12/31	sts2_vel:RT72A-08
	Laramie	L05	41.08	-105.59	1.8	2000/09/01	2001/12/31	sts2_vel:RT72A-08
	Laramie	L06	41.10	-105.61	7600	2000/09/01	2001/12/31	sts2_vel:RT72A-08
	Laramie	L07	41.12	-105.62	1.8	2000/09/01	2001/12/31	sts2_vel:RT72A-08
*	Laramie	L08	41.14	-105.64	7410	2000/09/01	2001/12/31	sts2_vel:RT72A-08
	Laramie	L09	41.16	-105.66	1.8	2000/09/01	2001/12/31	sts2_vel:RT72A-08
	Laramie	L10	41.18	-105.67	7630	2000/09/01	2001/12/31	sts2_vel:RT72A-08
*	Laramie	L11	41.20	-105.69	1.8	2000/09/01	2001/12/31	sts2_vel:RT72A-08
	Laramie	L12	41.22	-105.71	7250	2000/09/01	2001/12/31	sts2_vel:RT72A-08
	Laramie	L13	41.23	-105.73	7280	2000/09/01	2001/12/31	sts2_vel:RT72A-08
	Laramie	L14	41.26	-105.74	7310	2000/09/01	2001/12/31	sts2_vel:RT72A-08
	Laramie	L16	41.29	-105.79	1.8	2000/09/01	2001/12/31	sts2_vel:RT72A-08
	Laramie	L17	41.32	-105.79	7450	2000/09/01	2001/12/31	sts2_vel:RT72A-08
	Laramie	L18	41.33	-105.81	7540	2000/09/01	2001/12/31	sts2_vel:RT72A-08
*	Laramie	L19	41.36	-105.83	7260	2000/09/01	2001/12/31	sts2_vel:RT72A-08
	Laramie	L20	41.38	-105.84	7260	2000/09/01	2001/12/31	sts2_vel:RT72A-08
*	Laramie	L22	41.42	-105.88	7320	2000/09/01	2001/12/31	sts2_vel:RT72A-08
	Laramie	L23	41.44	-105.89	7360	2000/09/01	2001/12/31	sts2_vel:RT72A-08
	Laramie	L24	41.49	-105.89	1.8	2000/09/01	2001/12/31	sts2_vel:RT72A-08
	Laramie	L25	41.48	-105.93	1.8	2000/09/01	2001/12/31	sts2_vel:RT72A-08
	Laramie	L26	41.50	-105.95	1.8	2000/09/01	2001/12/31	sts2_vel:RT72A-08
	Laramie	L27	41.52	-105.96	1.8	2000/09/01	2001/12/31	sts2_vel:RT72A-08
	Laramie	L28	41.54	-105.98	7440	2000/09/01	2001/12/31	sts2_vel:RT72A-08
	Laramie	L29	41.56	-106.00	1.8	2000/09/01	2001/12/31	sts2_vel:RT72A-08
	Laramie	L30	41.59	-106.01	7330	2000/09/01	2001/12/31	sts2_vel:RT72A-08
	Laramie	L31	41.60	-106.03	7340	2000/09/01	2001/12/31	sts2_vel:RT72A-08

Best	Array	Station	Latitude	Longitude	Elevation (m)	Start Date	End Date	Instrumentation
*	CDROM	N00	42.46	-107.70	1945	1999/06/09	2000/12/31	STS2
	CDROM	N01	42.28	-107.60	2275	1999/06/09	2000/12/31	CMG3T
	CDROM	N02	42.15	-107.50	1983	1999/06/06	2000/12/31	STS2
*	CDROM	N04	41.98	-107.43	2002	1999/06/06	2000/12/31	CMG3T
*	CDROM	N05	41.89	-107.39	2077	1999/06/07	2000/12/31	STS2
	CDROM	N06	41.80	-107.35	2136	1999/06/06	2000/12/31	STS2
	CDROM	N07	41.72	-107.32	2133	1999/06/07	2000/12/31	CMG3T
	CDROM	N08	41.62	-107.28	2150	1999/06/07	2000/12/31	CMG3
*	CDROM	N09	41.54	-107.24	2147	1999/06/07	2000/12/31	CMG40T
	CDROM	N10	41.45	-107.21	2240	1999/06/07	2000/12/31	STS2
	CDROM	N12	41.25	-107.25	2270	1999/06/08	2000/12/31	STS2
	CDROM	N17	40.81	-106.94	2473	1999/06/12	2000/12/31	CMG3T
	CDROM	N21	40.45	-106.92	2064	1999/06/11	2000/12/31	STS2
	CDROM	N25	40.13	-106.70	2554	1999/06/11	2000/12/31	STS2
	CDROM	N26	40.05	-106.66	2642	1999/06/18	2000/12/31	STS2
	YellowStone	Y04	43.51	-111.9	1502	2000/06/28	2001/12/31	CMG40T
	YellowStone	Y05	43.19	-111.58	1970	2000/06/28	2001/12/31	CMG3T
*	YellowStone	Y07	42.56	-110.89	2155	2000/06/28	2001/12/31	STS2
*	YellowStone	Y22	42.59	-109.25	2574	2000/06/20	2001/12/31	STS2
*	YellowStone	Y31	43.74	-109.98	2789	2000/06/23	2001/12/31	STS2
*	YellowStone	Y32	43.58	-109.45	2138	2000/07/06	2001/12/31	STS2
*	YellowStone	Y33	43.23	-108.98	1756	2000/06/19	2001/12/31	CMG3T
	YellowStone	Y34	42.97	-108.56	1562	2000/06/20	2001/12/31	STS2
	YellowStone	Y35	42.57	-108.04	2062	2000/06/20	2001/12/31	STS2
	YellowStone	Y43	44.45	-109.6	1897	2000/06/20	2001/12/31	STS2
	YellowStone	Y44	44.1	-109.19	2121	2000/06/20	2001/12/31	STS2
	YellowStone	Y46	43.6	-108.2	1362	2000/06/30	2001/12/31	STS2
*	USARRAY	M20A	41.49	-108.19	2134	2007/11/02	2009/10/18	STS-2 G3 / Quanterra 330 Linear Phase Co
*	USARRAY	M21A	41.61	-107.36	2275	2007/11/01	2009/10/09	STS-2 G3 / Quanterra 330 Linear Phase Co
*	USARRAY	M22A	41.4	-106.6	2334	2007/11/25	2010/05/15	Guralp CMG3T/Quanterra 330 Linear Phase Composite
	USARRAY	M23A	41.47	-105.72	2166	2008/07/15	2010/05/13	Guralp CMG3T/Quanterra 330 Linear Phase Composite
	USARRAY	M23A	41.47	-105.72	2166	2008/07/15	2010/05/13	Guralp CMG3T/Quanterra 330 Linear Phase Composite
	USARRAY	N22A	40.80	-106.45	2472	2007/11/27	2010/06/11	Guralp CMG3T/Quanterra 330 Linear Phase Composite
	USARRAY	O20A	40.13	-108.24	1915	2007/11/12	Current	STS-2 G3 / Quanterra 330 Linear Phase Co
	USARRAY	O21A	40.21	-107.47	2343	2007/11/10	2009/11/05	STS-2 G3 / Quanterra 330 Linear Phase Co
	USARRAY	O22A	40.16	-106.55	2747	2008/06/21	2010/06/14	Guralp CMG3T/Quanterra 330 Linear Phase Composite
*	USARRAY	O23A	40.21	-105.92	2635	2008/07/06	2010/06/14	STS-2 G3 / Quanterra 330 Linear Phase Co

Best	Array	Station	Latitude	Longitude	Elevation (m)	Start Date	End Date	Instrumentation
	USARRAY	O24A	40.12	-105.07	1553	2008/07/03	2010/05/17	STS-2 G3 / Quanterra 330 Linear Phase Co
*	USARRAY	P20A	39.5	-108.39	1738	2007/12/08	2009/11/04	STS-2 G3 / Quanterra 330 Linear Phase Co
	USARRAY	P21A	39.52	-107.45	2097	2007/12/12	2009/10/22	STS-2 G3 / Quanterra 330 Linear Phase Co
	USARRAY	P22A	39.60	-106.76	2170	2008/06/22	2010/06/15	Guralp CMG3T/Quanterra 330 Linear Phase Composite
	USARRAY	P23A	39.37	-105.84	3006	2008/06/24	2010/06/24	Guralp CMG3T/Quanterra 330 Linear Phase Composite
	USARRAY	N23A	40.89	-105.94	2458	2008/07/05	Current	STS-2 G3 / Quanterra 330 Linear Phase Co
*	IM IMS	PD31	42.77	-109.56	2219	1970/01/24	Current	Geotech KS-54000 Borehole Seismometer
	DeepProbe	S101	42.45	-108.89	2431	1997/05/15	1997/12/31	CMG3T
	DeepProbe	S104	42.13	-108.91	2274	1997/05/15	1997/12/31	CMG3T
	DeepProbe	S105	42.06	-108.90	2289	1997/05/15	1997/12/31	GS13
*	DeepProbe	S107	41.90	-108.84	2103	1997/05/14	1997/12/31	CMG3T
	DeepProbe	S109	41.73	-108.92	2065	1997/05/12	1997/12/31	CMG3T
	DeepProbe	S111	41.54	-108.85	2092	1997/05/16	1997/12/31	CMG3T
	DeepProbe	S112	41.46	-108.85	2138	1997/05/12	1997/12/31	CMG3T
	DeepProbe	S113	41.37	-108.86	2133	1997/05/14	1997/12/31	CMG3T
	DeepProbe	S114	41.27	-108.81	2124	1997/05/12	1997/12/31	GS13
	DeepProbe	S116	41.11	-108.81	2230	1997/05/12	1997/12/31	CMG3T
	DeepProbe	S117	41.02	-108.83	2195	1997/05/14	1997/12/31	CMG3T
*	DeepProbe	S119	40.84	-108.91	1882	1997/05/09	1997/12/31	CMG3T
*	DeepProbe	S121	40.64	-108.83	2011	1997/05/08	1997/12/31	CMG3T
	DeepProbe	S125	40.26	-108.77	1849	1997/05/05	1997/12/31	CMG3T
	DeepProbe	S126	40.19	-108.73	1761	1997/05/05	1997/12/31	CMG3T / L22
*	DeepProbe	S129	39.91	-108.68	1929	1997/05/09	1997/12/31	CMG3T
*	DeepProbe	S130	39.84	-108.77	1932	1997/05/05	1997/12/31	CMG3T
*	DeepProbe	S131	39.75	-108.77	2072	1997/05/06	1997/12/31	CMG3T
	DeepProbe	S134	39.49	-108.77	1811	1997/05/08	1997/12/31	CMG3T
	DeepProbe	S137	39.21	-108.77	1401	1997/05/12	1997/12/31	CMG3T
	DeepProbe	S139	39.00	-108.74	2067	1997/05/12	1997/12/31	CMG3T
	DeepProbe	S224	40.22	-108.98	1819	1997/08/19	1997/12/31	CMG3T
	DeepProbe	S225	40.16	-108.87	1719	1997/08/19	1997/12/31	CMG3T
	DeepProbe	S226	40.06	-108.84	1645	1997/08/20	1997/12/31	CMG3T
	DeepProbe	S229	39.78	-108.60	1937	1997/08/18	1997/12/31	CMG3T
	DeepProbe	S230	39.69	-108.54	2681	1997/08/22	1997/12/31	CMG3T
	DeepProbe	S234	39.36	-108.15	1509	1997/08/13	1997/12/31	CMG3T
	DeepProbe	S235	39.27	-108.04	1948	1997/08/13	1997/12/31	CMG3T
*	USNSN	ISCO	39.8	-105.61	2743	2013/08/08	Current	STS2-I / CMG5TEX-N / CMG3V-N / CMG3H-N / EXT-S2G
*	InterMtnWest	PHWY	41.3	-105.46	2645	2004/10/11	Current	CMG3TESP-30S
*	InterMtnWest	RWWY	41.69	-107.21	2402	2004/09/09	Current	CMG3TESP-30S

Table 2. List of earthquakes used in the study. Complete list comprises earthquakes used for Group(B) data. Earthquakes with an * in the "Best" column were also used for Group(A) data.

Best	Event Time	Latitude	Longitude	Back Azimuth
	1997_113_19_44_28	13.986	144.901	293.16
	1997_123_16_45_44	-33	-178	234.103
	1997_141_14_10_26	-20.438	169.287	249.484
*	1997_145_23_22_32	-32.115	179.819	234.436
	1997_212_21_54_20	-6.565	130.866	286.163
	1997_225_04_45_02	26	128	311.009
	1997_247_04_23_37	-26.569	178.336	239.344
	1997_309_23_45_30	27.864	142.608	303.104
	1998_027_21_05_44	-22.411	179.035	241.954
	1998_038_01_18_59	24.821	141.746	301.034
	1998_104_03_41_22	-23.821	-179.871	240.265
	1999_207_01_33_21	-6.916	151.432	272.944
*	1999_238_07_39_25	-3.472	145.765	278.709
	1999_265_00_14_37	23.94	120.97	315.924
	1999_296_02_12_04	-4.779	153.327	272.775
*	1999_345_18_03_33	16.209	120.019	312.093
	2000_005_07_40_47	-11.27	165.25	260.791
*	2000_057_08_11_38	14.218	145.522	291.83
	2000_127_13_44_15	-10.7	165.37	261.158
*	2000_133_23_10_21	35.899	70.641	3.142
	2000_158_02_42_02	41.831	32.913	29.975
*	2000_166_02_15_21	-25.48	178.08	242.046
	2000_173_16_25_06	14.112	144.962	293.211
*	2000_199_22_53_19	35	74	355.89
*	2000_222_00_08_34	-18.47	166.923	254.141
*	2000_228_04_30_08	-31.511	179.725	236.521
*	2000_234_09_16_25	-53.08	-46.32	147.392
	2000_278_16_58_41	-15.348	167.158	256.656
*	2000_323_06_54_56	-5.26	151.7	274.369
	2000_330_18_10_47	40.167	49.954	18.517
*	2000_341_22_57_39	-4.75	152	274.605
*	2000_356_01_01_19	-5.814	152.197	272.3
	2001_129_17_38_26	-10.318	161.232	264.281
	2001_184_13_10_42	21.641	142.984	299.942
	2001_229_22_25_49	25.748	126.19	314.165
	2001_346_12_53_18	-17.189	167.721	254.663
	2002_116_16_06_03	13.186	144.842	292.616
	2002_154_09_15_00	27.564	139.78	306.179
	2002_181_21_29_36	-22.201	179.25	243.788
	2002_214_23_11_39	29.28	138.97	307.884
	2003_117_16_03_40	-20.944	169.773	250.491
	2003_124_20_08_46	-30.587	-178.29	236.072
*	2003_133_21_21_09	-17.407	167.822	254.431
	2003_203_04_21_40	-15.416	166.142	257.012
	2003_206_09_37_45	-1.528	149.694	278.31
	2005_036_03_34_23	15.991	145.93	293.94
	2005_039_14_48_09	-14.193	167.29	257.259
	2005_288_15_50_59	25.353	123.345	316.007
	2006_160_05_58_27	-17.531	-178.747	245.968
*	2006_187_03_57_50	39.119	71.836	2.024
*	2006_219_22_18_52	-15.64	168.01	255.693

Best	Event Time	Latitude	Longitude	Back Azimuth
	2006_360_12_26_21	21.799	120.547	315.104
	2007_094_11_00_25	-20.741	168.803	251.228
	2007_111_07_12_44	-3.456	151.308	275.749
	2007_149_01_03_27	-4.587	151.841	273.855
	2007_165_17_41_04	-5.649	151.563	273.862
	2007_238_12_37_31	-17.457	-174.335	241.921
	2007_271_13_38_57	22.013	142.668	299.383
	2007_278_07_17_51	-24.988	179.466	241.58
	2007_289_21_05_43	-25.775	179.53	240.954
	2008_109_20_39_07	-17.342	-179.022	246.284
	2008_110_05_58_40	-20.174	168.882	251.626
	2008_119_18_33_34	-19.941	168.953	250.225
*	2008_130_21_51_25	11.202	142.724	291.047
*	2008_153_01_57_21	20.24	121.29	313.47
	2008_167_01_13_11	-17.735	-179.733	246.451
*	2008_197_03_26_21	34.827	28.799	36.128
	2008_202_21_30_29	27.773	139.615	306.429
*	2008_218_09_49_17	32.756	105.494	333.544
	2008_337_12_31_43	19.108	145.75	295.704
	2009_116_00_06_53	-30.3	-178.582	236.456
*	2009_194_18_05_01	24.056	122.201	316.091
	2009_230_21_20_47	-26.064	-178.391	239.682
	2009_246_13_26_17	31.14	130.014	313.765
*	2010_079_14_00_49	-3.361	152.245	275.211
	2010_173_22_16_20	-19.201	-177.553	243.978
*	2010_222_23_18_31	-14.46	167.345	257.017
	2010_223_03_35_19	-17.403	167.814	254.755
	2010_228_19_35_49	-20.799	-178.826	243.621
*	2011_012_21_32_53	26.973	139.882	305.702
*	2011_013_16_16_41	-20.628	168.471	251.514
*	2011_052_10_57_52	-26.142	178.394	241.611
	2011_066_00_09_36	-10.349	160.766	264.308
*	2011_108_13_03_02	-34.336	179.874	234.281
*	2011_130_08_55_08	-20.244	168.226	251.963
	2011_172_02_04_15	-11.479	165.551	260.442
*	2011_200_19_35_43	40.081	71.41	2.322
	2011_201_22_04_59	-10.34	162.01	263.859
	2011_210_07_42_23	-23.801	179.751	242.29
	2011_312_02_59_08	27.324	125.621	315.541
*	2012_024_00_52_05	-24.977	178.52	242.394
	2012_147_21_48_10	26.91	140.055	305.635
	2012_181_21_07_33	43.433	84.7	352.455
	2012_188_02_28_22	-14.657	167.34	256.868
	2012_210_20_03_56	-4.651	153.173	273.601
	2012_224_12_23_18	38.329	46.826	21.616
	2013_110_00_02_47	30.308	102.888	333.552
	2013_111_03_22_16	29.933	138.887	308.389
*	2013_166_11_20_36	-33.853	179.402	234.913
	2013_202_23_45_56	34.512	104.262	335.456
	2013_218_16_46_18	-16.86	167.311	255.122
*	2013_240_02_54_41	-27.754	179.62	239.418

Table 3. List of signals used in the study. Complete list comprises signals used for Group(B) data. Signals with an * in the "Best" column were also used for Group(A) data.

Best	Event Time	Station	Event Latitude	Event Longitude	Back Azimuth	Signal / Noise	δt	δt error	ϕ	ϕ error	dof
	1997_113_19_44_28	ISCO	13.986	144.901	293.16	2.945	3.053	1.442	23.614	3.332	38
	1997_123_16_45_44	ISCO	-33	-178	234.103	4.608	3.35	NaN	151	NaN	16
	1997_141_14_10_26	S107	-20.438	169.287	249.484	5.435	1.279	NaN	87.01	NaN	37
	1997_141_14_10_26	S111	-20.438	169.287	249.436	5.677	1.228	NaN	12.966	NaN	32
	1997_141_14_10_26	S112	-20.438	169.287	249.427	5.25	1.076	NaN	15.667	NaN	29
	1997_141_14_10_26	S113	-20.438	169.287	249.408	4.241	3.682	0.711	163.261	2.854	44
	1997_141_14_10_26	S114	-20.438	169.287	249.425	2.65	1.786	NaN	12.788	NaN	227
	1997_141_14_10_26	S116	-20.438	169.287	249.41	4.318	3.761	0.555	163.548	2.135	34
	1997_141_14_10_26	S117	-20.438	169.287	249.382	2.98	1.883	2.1	1.219	45	11
	1997_141_14_10_26	S119	-20.438	169.287	249.316	4.367	2.1	2.1	0.005	45	9
	1997_141_14_10_26	S121	-20.438	169.287	249.338	4.21	1.621	2.1	4.372	45	7
	1997_141_14_10_26	S129	-20.438	169.287	249.346	5.264	1.352	NaN	5.629	NaN	37
	1997_141_14_10_26	S130	-20.438	169.287	249.282	5.203	1.333	NaN	13.396	NaN	14
	1997_141_14_10_26	S131	-20.438	169.287	249.275	4.574	1.735	2.1	7.362	45	14
	1997_141_14_10_26	S134	-20.438	169.287	249.243	3.257	2.1	2.1	0.005	45	11
	1997_141_14_10_26	S137	-20.438	169.287	249.212	4.55	3.298	NaN	97.706	NaN	27
	1997_145_23_22_32	S101	-32.115	179.819	234.436	6.25	0.8	NaN	66	NaN	29
	1997_145_23_22_32	S104	-32.115	179.819	234.389	5.015	1.881	0.84	59.924	2.521	37
	1997_145_23_22_32	S105	-32.115	179.819	234.386	2.609	1.9	NaN	61	NaN	108
*	1997_145_23_22_32	S107	-32.115	179.819	234.397	5.179	1.206	0.608	59.87	3.513	37
	1997_145_23_22_32	S109	-32.115	179.819	234.332	5.359	0.25	NaN	5	NaN	33
	1997_145_23_22_32	S111	-32.115	179.819	234.351	4.858	2.25	NaN	59	NaN	32
	1997_145_23_22_32	S112	-32.115	179.819	234.341	5.213	1.6	NaN	152	NaN	43
	1997_145_23_22_32	S113	-32.115	179.819	234.323	4.582	3.15	NaN	61	NaN	34
	1997_145_23_22_32	S116	-32.115	179.819	234.324	3.391	3.786	0.539	66.653	3.13	39
	1997_145_23_22_32	S117	-32.115	179.819	234.298	3.112	3.138	1.096	65.214	3.961	34
*	1997_145_23_22_32	S119	-32.115	179.819	234.234	3.267	0.777	0.381	-12.242	13.753	42
*	1997_145_23_22_32	S121	-32.115	179.819	234.256	3.96	2.137	0.468	66.974	4.082	24
*	1997_145_23_22_32	S129	-32.115	179.819	234.264	4.464	0.518	0.248	82.24	17.616	38
	1997_145_23_22_32	S130	-32.115	179.819	234.204	3.055	1.271	0.555	72.19	8.803	21
*	1997_145_23_22_32	S131	-32.115	179.819	234.197	4.214	1.206	0.311	69.75	4.746	44
	1997_145_23_22_32	S134	-32.115	179.819	234.167	2.995	2.4	NaN	62	NaN	26
	1997_145_23_22_32	S137	-32.115	179.819	234.139	5.465	1.654	2.1	6.439	45	10
	1997_145_23_22_32	S139	-32.115	179.819	234.138	4.997	3.371	0.983	61.989	6.144	29
	1997_212_21_54_20	S107	-6.565	130.866	286.163	2.548	1.605	NaN	-22.221	NaN	51
	1997_225_04_45_02	CALI	26	128	311.006	2.975	0.899	0.391	110.721	10.444	46
	1997_225_04_45_02	CSD	26	128	311.212	2.672	0.587	1.018	78.401	42.961	36
	1997_225_04_45_02	DOUG	26	128	310.937	2.634	1.735	0.724	116.599	7.425	27
	1997_225_04_45_02	GRAN	26	128	311.006	2.938	2.4	NaN	125	NaN	33
	1997_225_04_45_02	HIAW	26	128	310.936	2.59	2.7	NaN	33	NaN	32
	1997_225_04_45_02	ISCO	26	128	313.029	4.765	2.971	1.616	44.446	19.024	41
	1997_225_04_45_02	JNMT	26	128	311.394	3.412	0.49	0.311	95.056	32.404	41
	1997_225_04_45_02	JWM	26	128	310.996	2.939	1.531	0.602	122.173	4.825	48
	1997_225_04_45_02	LIME	26	128	310.89	2.817	3.022	1.448	42.853	4.381	26
	1997_225_04_45_02	LOOK	26	128	311.101	2.85	1.85	NaN	44	NaN	32
	1997_225_04_45_02	NDH	26	128	311.306	2.632	3.647	NaN	43.53	NaN	44
	1997_225_04_45_02	PMR	26	128	310.88	3.459	2.722	1.679	39.322	4.01	39
	1997_225_04_45_02	RRE	26	128	310.947	3.632	3.024	0.555	30.636	2.906	35
	1997_225_04_45_02	RRW	26	128	310.857	3.165	4.2	NaN	38	NaN	33
	1997_225_04_45_02	S101	26	128	310.91	2.931	1.905	NaN	-1.815	NaN	18
	1997_225_04_45_02	S121	26	128	310.841	2.941	1.2	NaN	122	NaN	28
	1997_225_04_45_02	S125	26	128	310.858	2.935	1.373	NaN	-0.962	NaN	19
	1997_225_04_45_02	S126	26	128	310.88	3.746	2.7	NaN	45	NaN	14
	1997_225_04_45_02	S131	26	128	310.819	2.854	1.507	NaN	-6.99	NaN	13
	1997_225_04_45_02	S137	26	128	310.773	5.443	1.277	NaN	3.666	NaN	30
	1997_225_04_45_02	S234	26	128	311.213	3.06	2.691	0.483	139.013	2.631	49
	1997_225_04_45_02	SMR	26	128	311.216	3.598	3.348	1.044	37.066	4.526	18
	1997_225_04_45_02	TANK	26	128	310.891	3.146	0.554	0.297	80.529	31.862	31
	1997_225_04_45_02	VMCK	26	128	310.957	3.353	4.078	0.189	51	2.828	32
	1997_225_04_45_02	YSCF	26	128	311.106	2.597	4.2	NaN	43	NaN	26
	1997_225_04_45_02	ZENO	26	128	310.845	3.076	1.141	0.676	116.485	9.771	32
	1997_247_04_23_37	CALA	-26.569	178.336	239.344	4.866	2.041	0.836	61.608	2.563	32
	1997_247_04_23_37	CALI	-26.569	178.336	239.344	3.874	2.9	NaN	68	NaN	30
	1997_247_04_23_37	CSD	-26.569	178.336	239.525	3.398	1.85	NaN	152	NaN	67
	1997_247_04_23_37	DOUG	-26.569	178.336	239.285	4.818	0.6	NaN	-24	NaN	17
	1997_247_04_23_37	DRY	-26.569	178.336	239.388	2.619	1.063	0.254	170.122	7.895	31
	1997_247_04_23_37	GRAN	-26.569	178.336	239.356	3.292	0.531	0.372	-10.065	16.877	48

Best	Event Time	Station	Event Latitude	Event Longitude	Back Azimuth	Signal / Noise	δt	δt error	ϕ	ϕ error	dof
	1997_247_04_23_37	HELL	-26.569	178.336	239.391	3.559	0.545	0.38	-7.511	19.177	44
	1997_247_04_23_37	HIAW	-26.569	178.336	239.291	3.898	0.294	0.263	20.165	43.247	40
	1997_247_04_23_37	JNMT	-26.569	178.336	239.685	3.762	1.642	0.231	47.64	3.676	30
	1997_247_04_23_37	JWM	-26.569	178.336	239.337	3.231	0.9	NaN	165	NaN	35
	1997_247_04_23_37	KINN	-26.569	178.336	239.392	3.317	0.66	0.326	167.282	10.292	51
	1997_247_04_23_37	LANG	-26.569	178.336	239.553	2.503	2.198	1.307	72.888	39.296	27
	1997_247_04_23_37	LIME	-26.569	178.336	239.248	3.297	4.2	NaN	65	NaN	32
	1997_247_04_23_37	LSC	-26.569	178.336	239.434	5.106	1.25	NaN	63	NaN	25
	1997_247_04_23_37	MAYB	-26.569	178.336	239.581	2.731	3.751	0.553	65.863	2.838	60
	1997_247_04_23_37	NDH	-26.569	178.336	239.607	3.819	2.75	NaN	144	NaN	26
	1997_247_04_23_37	PINR	-26.569	178.336	239.465	2.843	3.25	NaN	153	NaN	46
	1997_247_04_23_37	PMR	-26.569	178.336	239.243	2.97	3.944	0.344	67.308	3.18	39
	1997_247_04_23_37	POW	-26.569	178.336	239.478	2.889	4.2	NaN	148	NaN	31
	1997_247_04_23_37	RRE	-26.569	178.336	239.305	2.633	0.45	NaN	-17	NaN	42
	1997_247_04_23_37	RRW	-26.569	178.336	239.224	2.993	3.856	0.449	69.17	3.325	38
	1997_247_04_23_37	S125	-26.569	178.336	239.212	4.707	1.289	NaN	66.625	NaN	33
	1997_247_04_23_37	S225	-26.569	178.336	239.142	5.185	3.159	0.321	67.237	1.942	37
	1997_247_04_23_37	S226	-26.569	178.336	239.155	4.068	4.2	NaN	152	NaN	28
	1997_247_04_23_37	S230	-26.569	178.336	239.309	3.945	2.135	0.425	71.26	2.963	38
	1997_247_04_23_37	S234	-26.569	178.336	239.52	3.289	1.9	NaN	66	NaN	27
	1997_247_04_23_37	S235	-26.569	178.336	239.58	2.727	2.5	NaN	156	NaN	24
	1997_247_04_23_37	SMR	-26.569	178.336	239.534	2.566	2.4	NaN	65	NaN	42
	1997_247_04_23_37	SUTT	-26.569	178.336	239.532	3.627	1.608	0.42	52.453	2.689	49
	1997_247_04_23_37	SWB	-26.569	178.336	239.48	3.112	0.8	NaN	-18	NaN	31
	1997_247_04_23_37	TANK	-26.569	178.336	239.243	4.375	3.284	0.311	68.658	1.988	38
	1997_247_04_23_37	YSCF	-26.569	178.336	239.432	3.536	2.52	0.263	69.457	2.133	50
	1997_247_04_23_37	ZENO	-26.569	178.336	239.204	3.796	4.05	NaN	62	NaN	35
	1997_309_23_45_30	JNMT	27.864	142.608	303.104	2.539	3.514	0.638	99.327	6.343	18
	1997_309_23_45_30	S229	27.864	142.608	302.792	2.683	3.102	0.467	105.313	3.483	45
	1997_309_23_45_30	SWB	27.864	142.608	302.87	2.739	2.77	0.842	101.176	8.468	25
	1998_027_21_05_44	CALI	-22.411	179.035	241.941	3.153	4.15	0.097	160	3.361	38
	1998_027_21_05_44	JNMT	-22.411	179.035	242.29	3.188	4.2	NaN	-26	NaN	22
	1998_027_21_05_44	LIME	-22.411	179.035	241.815	3.538	3.485	0.852	160.49	4.994	18
	1998_027_21_05_44	MAYB	-22.411	179.035	242.181	2.942	4.011	0.28	161.861	4.618	35
	1998_027_21_05_44	NDH	-22.411	179.035	242.214	4.48	3.563	1.306	153.48	7.368	21
	1998_027_21_05_44	PMR	-22.411	179.035	241.799	3.407	2.285	0.666	82.953	20.709	23
	1998_027_21_05_44	RRW	-22.411	179.035	241.776	3.111	4.076	0.185	163.5	3.124	49
	1998_027_21_05_44	SUTT	-22.411	179.035	242.125	4.046	2.862	1.77	152.736	6.993	20
	1998_027_21_05_44	TANK	-22.411	179.035	241.834	2.91	3.937	0.371	162.63	4.415	22
	1998_027_21_05_44	YSCF	-22.411	179.035	242.029	3.308	3.46	0.852	160.154	3.649	38
	1998_038_01_18_59	DOUG	24.821	141.746	301.034	2.607	3.029	1.072	103.285	8.778	15
	1998_038_01_18_59	JNMT	24.821	141.746	301.46	2.53	0.571	0.423	89.615	28.366	17
	1998_104_03_41_22	BLUE	-23.821	-179.871	240.265	2.64	0.85	NaN	-17	NaN	11
	1998_104_03_41_22	CALI	-23.821	-179.871	240.228	3.381	1.542	0.459	70.363	3.846	28
	1998_104_03_41_22	FWGP	-23.821	-179.871	240.119	2.723	0.512	0.486	21.898	43.998	25
	1998_104_03_41_22	GRAN	-23.821	-179.871	240.205	3.061	3.25	NaN	-34	NaN	23
	1998_104_03_41_22	HELL	-23.821	-179.871	240.244	2.59	3.299	1.197	147.526	5.116	29
	1998_104_03_41_22	JNMT	-23.821	-179.871	240.576	2.614	1.943	0.463	46.774	5.92	17
	1998_104_03_41_22	LSC	-23.821	-179.871	240.313	2.51	1.8	NaN	65	NaN	24
	1998_104_03_41_22	PD31	-23.821	-179.871	239.67	2.797	0.15	NaN	86	NaN	27
	1998_104_03_41_22	PINR	-23.821	-179.871	240.354	3.281	3.4	NaN	64	NaN	21
	1998_104_03_41_22	RRE	-23.821	-179.871	240.149	2.542	3.576	0.702	144.397	3.544	87
	1998_104_03_41_22	TANK	-23.821	-179.871	240.122	2.631	2.76	0.699	68.85	4.58	26
	1998_104_03_41_22	TWIN	-23.821	-179.871	240.357	2.618	1.7	NaN	66	NaN	20
	1998_104_03_41_22	YSCF	-23.821	-179.871	240.317	2.656	2.412	0.604	68.132	3.83	31
	2000_057_08_11_38	N04	14.218	145.522	291.83	3.292	2.12	0.716	31.221	3.4	26
	2000_057_08_11_38	N08	14.218	145.522	291.918	2.663	2.9	NaN	-72	NaN	10
*	2000_057_08_11_47	N04	13.94	144.65	292.228	3.2	2.183	0.737	31.277	3.408	27
	2000_057_08_11_47	N05	13.94	144.65	292.251	3.045	2.252	1.356	28.371	4.26	20
	2000_057_08_11_47	N06	13.94	144.65	292.27	2.878	1.565	NaN	-9	NaN	6
	2000_127_13_44_15	ISCO	-10.7	165.37	261.158	7.796	2.579	0.963	84.911	1.554	26
*	2000_133_23_10_21	ISCO	35.899	70.641	3.142	2.657	0.883	0.31	54.497	20.649	37
*	2000_133_23_10_21	N00	35.899	70.641	1.379	2.612	1.294	0.403	76.648	7.541	28
*	2000_166_02_15_25	ISCO	-25.516	178.046	242.039	4.718	2.548	0.429	71.288	2.35	33
*	2000_166_02_15_26	PD31	-24.98	178.38	240.006	3.217	1.25	NaN	64	NaN	82
	2000_173_16_25_06	ISCO	14.112	144.962	293.211	2.902	3.959	0.348	24.439	2.904	51
	2000_199_22_53_19	Y07	35	74	355.89	2.694	2.1	2.1	0.005	45	37

Best	Event Time	Station	Event Latitude	Event Longitude	Back Azimuth	Signal / Noise	δt	δt error	ϕ	ϕ error	dof
	2000_199_22_53_19	Y43	35	74	356.993	3.62	2.554	1.915	1.781	45	25
	2000_199_22_53_43	Y07	36.466	70.836	358.585	2.844	2.1	2.1	0.005	45	23
*	2000_199_22_53_43	Y22	36.466	70.836	359.928	3.461	0.989	0.456	73.031	7.533	39
*	2000_199_22_53_43	Y33	36.466	70.836	0.154	2.536	1.019	0.253	64.234	7.797	35
	2000_199_22_53_43	Y34	36.466	70.836	0.495	2.973	4.092	0.179	97.548	3.218	45
	2000_199_22_53_43	Y46	36.466	70.836	0.786	2.604	2.1	2.1	0.005	45	21
*	2000_222_00_08_34	ISCO	-18.47	166.923	254.141	4.061	2.319	0.907	80.622	3.895	19
*	2000_228_04_30_08	ISCO	-31.511	179.725	236.521	4.478	2.289	0.557	66.178	3.077	27
*	2000_228_04_30_08	Y04	-31.52	179.73	233.173	3.395	1.698	0.568	65.138	5.579	19
*	2000_228_04_30_08	Y07	-31.52	179.73	233.707	2.858	2.244	0.32	65.403	3.883	33
*	2000_228_04_30_08	Y22	-31.52	179.73	234.714	3.692	0.926	0.25	131.063	4.858	41
*	2000_228_04_30_08	Y31	-31.52	179.73	234.402	2.574	1.205	0.308	126	5.332	40
*	2000_228_04_30_08	Y32	-31.52	179.73	234.714	3.098	1.039	0.219	81.072	6.11	40
*	2000_228_04_30_08	Y33	-31.52	179.73	234.963	3.696	0.844	0.194	84.284	8.759	37
*	2000_234_09_16_25	ISCO	-53.08	-46.32	147.392	4.831	0.857	0.148	22.766	8.763	46
	2000_278_16_58_41	L28	-15.348	167.158	256.441	2.926	1.354	NaN	-11.396	NaN	39
	2000_278_16_58_41	L29	-15.348	167.158	256.433	3.315	1.266	NaN	-3.248	NaN	55
	2000_278_16_58_41	L30	-15.348	167.158	256.427	3.994	0.908	1.071	101.107	32.175	39
*	2000_323_06_54_56	L22	-5.26	151.7	274.274	2.564	0.822	1.618	-36.009	45	35
	2000_323_06_54_56	Y07	-5.26	151.7	271.121	2.688	2.043	2.1	2.011	45	17
	2000_330_18_10_47	L12	40.167	49.954	18.517	3.087	2.406	NaN	92.764	NaN	25
	2000_341_22_57_39	L02	-4.75	152	274.605	3.321	1.338	NaN	-16.51	NaN	33
	2000_341_22_57_39	L03	-4.75	152	274.598	3.159	1.15	NaN	-81	NaN	14
	2000_341_22_57_39	L04	-4.75	152	274.591	2.835	0.7	NaN	-80	NaN	39
	2000_341_22_57_39	L05	-4.75	152	274.585	2.541	1.598	2.1	-4.727	45	24
	2000_341_22_57_39	L16	-4.75	152	274.496	2.844	0.955	0.58	139.852	33.939	34
*	2000_341_22_57_39	L19	-4.75	152	274.486	2.727	0.849	0.314	132.674	19.988	24
	2000_341_22_57_39	Y33	-4.75	152	272.708	3.608	1.644	2.1	-1.404	45	35
	2000_341_22_57_39	Y34	-4.75	152	272.949	3.961	1.342	2.1	-4.312	45	15
	2000_356_01_01_19	Y35	-5.814	152.197	272.3	2.804	1.845	2.1	97.546	90.5	21
	2000_356_01_01_24	L01	-5.98	150.9	274.392	3.259	0.657	0.83	131.132	50.255	19
	2000_356_01_01_24	L02	-5.98	150.9	274.388	3.085	0.704	0.699	134.112	48.064	16
	2000_356_01_01_24	L10	-5.98	150.9	274.339	2.699	0.814	0.768	130.615	40.389	13
*	2000_356_01_01_24	PD31	-5.98	150.9	272.064	2.549	0.236	0.163	139.015	38.295	43
	2000_356_01_01_24	Y34	-5.98	150.9	272.787	2.897	4.2	NaN	6	NaN	14
	2000_356_01_01_30	L01	-6.169	149.353	275.282	3.146	0.6	NaN	114	NaN	23
*	2000_356_01_01_30	L02	-6.169	149.353	275.278	3.089	0.677	0.669	136.501	49.028	17
*	2000_356_01_01_30	L08	-6.169	149.353	275.24	2.551	0.967	0.759	136.876	38.963	16
	2000_356_01_01_30	L10	-6.169	149.353	275.232	2.585	0.779	0.631	131.122	35.755	13
*	2000_356_01_01_30	L11	-6.169	149.353	275.222	2.691	0.758	0.803	130.959	43.707	24
	2000_356_01_01_30	Y04	-6.169	149.353	271.519	2.643	1.5	NaN	83	NaN	18
	2000_356_01_01_30	Y05	-6.169	149.353	271.677	2.681	0.65	NaN	75	NaN	22
	2000_356_01_01_30	Y34	-6.169	149.353	273.71	3.296	0.3	NaN	-23	NaN	13
	2001_184_13_10_42	ISCO	21.641	142.984	299.942	2.894	0.608	0.59	73.143	49.223	32
	2001_346_12_53_18	ISCO	-17.189	167.721	254.663	3.161	1.15	NaN	-6	NaN	31
	2002_154_09_15_00	ISCO	27.564	139.78	306.179	2.974	0.846	0.543	80.384	38.28	13
	2002_181_21_29_36	ISCO	-22.201	179.25	243.788	4.47	2.701	0.352	74.174	2.203	37
	2002_214_23_11_39	ISCO	29.28	138.97	307.884	3.651	1.025	0.204	77.924	10.64	32
	2003_117_16_03_40	ISCO	-20.944	169.773	250.491	2.841	2.062	1.209	78.421	5.55	41
	2003_124_20_08_46	ISCO	-30.587	-178.29	236.072	3.598	1.269	1.753	86.767	42.314	36
*	2003_133_21_21_09	ISCO	-17.407	167.822	254.431	6.032	2.317	0.483	79.891	1.59	37
	2003_203_04_21_40	ISCO	-15.416	166.142	257.012	4.702	1.958	0.632	82.333	3.129	25
	2005_036_03_34_23	ISCO	15.991	145.93	293.94	3.901	2.8	NaN	12	NaN	53
	2005_039_14_48_09	ISCO	-14.193	167.29	257.259	6.671	4.2	NaN	173	NaN	25
	2005_288_15_50_59	ISCO	25.353	123.345	316.007	3.884	1.562	NaN	-37.797	NaN	16
	2006_160_05_58_27	ISCO	-17.531	-178.747	245.968	2.725	2.471	NaN	14.123	NaN	20
*	2006_187_03_57_50	ISCO	39.119	71.836	2.024	3.097	1.015	0.283	30.745	10.204	36
*	2006_219_22_18_52	ISCO	-15.64	168.01	255.693	6.823	2.129	0.483	81.764	2.523	25
	2006_219_22_18_52	RWWY	-15.64	168.01	254.907	3.537	0.45	NaN	112	NaN	18
	2006_360_12_26_21	RWWY	21.799	120.547	315.104	2.929	3.05	NaN	147	NaN	22
	2007_094_11_00_25	ISCO	-20.741	168.803	251.228	4.495	2.563	1.327	76.615	3.693	18
	2007_111_07_12_44	RWWY	-3.456	151.308	275.071	2.687	1.132	0.539	118.212	12.527	25
	2007_149_01_03_27	RWWY	-4.587	151.841	273.855	2.642	1.08	1.436	108.405	37.544	27
	2007_165_17_41_04	ISCO	-5.649	151.563	273.862	3.014	0.829	NaN	-52.747	NaN	28
	2007_238_12_37_31	RWWY	-17.457	-174.335	241.921	2.671	2.331	0.424	36.86	5.152	21
	2007_271_13_38_57	RWWY	22.013	142.668	299.383	3.403	1.192	0.392	57.311	11.049	30
	2007_278_07_17_51	ISCO	-24.988	179.466	241.58	2.8	1.627	NaN	52.553	NaN	30

Best	Event Time	Station	Event Latitude	Event Longitude	Back Azimuth	Signal / Noise	δt	δt error	ϕ	ϕ error	dof
	2007_278_07_17_51	PHWY	-24.988	179.466	241.799	3.653	1.281	NaN	72.776	NaN	46
	2007_289_21_05_43	ISCO	-25.775	179.53	240.954	3.673	2.12	0.443	69.342	3.019	51
	2007_289_21_05_43	PHWY	-25.775	179.53	241.183	4.86	1.591	0.456	69.346	3.18	32
	2007_289_21_05_43	RWWY	-25.775	179.53	240.125	2.973	0.896	0.639	78.17	14.072	29
	2008_109_20_39_07	ISCO	-17.342	-179.022	246.284	3.025	1.701	1.576	-10.854	11.531	30
	2008_109_20_39_07	PHWY	-17.342	-179.022	246.365	2.785	1.15	NaN	-17	NaN	53
	2008_110_05_58_40	ISCO	-20.174	168.882	251.626	3.423	2.659	1.034	78.214	3.993	30
	2008_119_18_33_34	PHWY	-19.941	168.953	252.097	3.065	3.65	NaN	-13.53	NaN	24
*	2008_130_21_51_25	M20A	11.202	142.724	291.047	3.804	0.7	0.29	143.989	17.491	20
*	2008_130_21_51_25	M21A	11.202	142.724	291.63	4.402	2.648	0.6	106.431	2.949	24
*	2008_130_21_51_25	N22A	11.202	142.724	292.162	2.502	0.615	0.423	44.104	17.228	39
	2008_130_21_51_25	RWWY	11.202	142.724	291.746	3.514	2.89	1.626	30.034	3.723	23
*	2008_153_01_57_21	M21A	20.24	121.29	313.47	2.921	0.433	0.104	85.54	13.54	38
	2008_167_01_13_11	ISCO	-17.735	-179.733	246.451	3.371	2.467	0.945	73.602	4.614	22
	2008_167_01_13_11	M20A	-17.735	-179.733	244.741	2.734	2.049	0.45	75.059	3.635	34
	2008_167_01_13_11	M21A	-17.735	-179.733	245.288	3.202	1.694	NaN	-16.408	NaN	33
	2008_167_01_13_11	M22A	-17.735	-179.733	245.8	2.86	3.513	0.503	70.47	2.082	88
	2008_167_01_13_11	N22A	-17.735	-179.733	245.898	2.655	0.698	0.212	199.927	20.278	42
	2008_167_01_13_11	O20A	-17.735	-179.733	244.744	2.666	4.15	NaN	61	NaN	40
	2008_167_01_13_11	PHWY	-17.735	-179.733	246.55	4.42	1.931	0.384	74.893	2.549	41
	2008_197_03_26_21	ISCO	34.827	28.799	36.128	4.027	0.843	0.395	51.345	8.12	47
	2008_197_03_26_21	M20A	34.827	28.799	34.255	2.803	0.806	0.332	101.481	11.294	46
	2008_197_03_26_21	M21A	34.827	28.799	34.831	2.521	0.717	0.248	68.691	15.516	53
	2008_197_03_26_21	M22A	34.827	28.799	35.377	2.612	0.896	0.13	92.892	5.094	142
	2008_197_03_26_21	N23A	34.827	28.799	35.851	2.667	0.89	0.509	109.446	10.628	64
	2008_197_03_26_21	O21A	34.827	28.799	34.819	3.243	1.09	0.121	68.444	5.092	56
	2008_197_03_26_21	O22A	34.827	28.799	35.465	3.479	1.879	0.48	112.659	3.924	61
	2008_197_03_26_21	O23A	34.827	28.799	35.899	2.923	1.229	0.212	55.5	4.126	84
	2008_197_03_26_21	O24A	34.827	28.799	36.485	2.975	0.816	0.269	98.183	11.894	83
*	2008_197_03_26_21	P20A	34.827	28.799	34.213	2.815	1.512	0.318	52.279	4.789	47
	2008_197_03_26_21	P22A	34.827	28.799	35.347	3.018	0.823	0.298	91.351	17.604	38
	2008_197_03_26_34	ISCO	35.8	27.86	36.227	3.695	0.751	0.485	54.626	13.615	35
	2008_197_03_26_34	M20A	35.8	27.86	34.409	2.949	0.776	0.3	101.359	10.643	46
	2008_197_03_26_34	M21A	35.8	27.86	34.975	2.677	0.715	0.255	68.934	15.671	50
	2008_197_03_26_34	M22A	35.8	27.86	35.509	2.692	0.848	0.131	91.535	5.796	135
	2008_197_03_26_34	N23A	35.8	27.86	35.968	2.684	0.853	0.525	109.107	11.654	59
	2008_197_03_26_34	O20A	35.8	27.86	34.421	3.159	0.909	0.276	65	11.798	30
	2008_197_03_26_34	O21A	35.8	27.86	34.948	3.121	1.086	0.125	68.829	4.887	60
	2008_197_03_26_34	O22A	35.8	27.86	35.581	3.047	1.903	0.555	112.8	4.148	61
	2008_197_03_26_34	O23A	35.8	27.86	36.007	2.86	1.297	0.226	55.472	4.144	79
	2008_197_03_26_34	O24A	35.8	27.86	36.58	2.885	0.836	0.317	98.424	13.738	65
	2008_197_03_26_34	P20A	35.8	27.86	34.346	2.525	1.612	0.379	51.243	5.057	45
	2008_197_03_26_34	P21A	35.8	27.86	34.991	3.488	1.121	0.321	57.479	7.426	26
	2008_197_03_26_34	P22A	35.8	27.86	35.459	3.008	0.848	0.376	93.012	19.49	29
	2008_197_03_26_34	P23A	35.8	27.86	36.091	3.033	1.896	0.456	46.034	3.277	44
	2008_202_21_30_29	ISCO	27.773	139.615	306.429	3.465	1.041	0.176	73.224	7.249	35
	2008_202_21_30_29	M21A	27.773	139.615	305.273	3.525	0.662	0.205	71.575	15.669	17
	2008_202_21_30_29	M22A	27.773	139.615	305.773	3.06	0.432	0.264	59.778	17.9	43
	2008_202_21_30_29	N23A	27.773	139.615	306.204	2.644	0.684	0.218	64.352	11.642	41
	2008_202_21_30_29	O20A	27.773	139.615	304.771	2.869	0.698	0.279	60.757	12.059	37
	2008_202_21_30_29	O21A	27.773	139.615	305.251	3.262	1.137	0.152	46.45	2.198	71
	2008_202_21_30_29	O22A	27.773	139.615	305.834	2.651	1.148	0.357	61.477	10.271	27
	2008_202_21_30_29	O24A	27.773	139.615	306.771	3.383	0.812	0.127	86.551	9.052	54
	2008_202_21_30_29	P20A	27.773	139.615	304.698	2.794	1.823	NaN	-6.629	NaN	143
	2008_202_21_30_29	P23A	27.773	139.615	306.29	2.576	2.023	0.899	118.138	4.619	28
	2008_202_21_30_29	PHWY	27.773	139.615	306.509	3.339	1.158	0.166	93.13	5.724	49
	2008_202_21_30_29	RWWY	27.773	139.615	305.368	2.61	1.247	0.316	62.817	7.56	21
*	2008_218_09_49_17	ISCO	32.756	105.494	333.544	2.886	0.722	0.685	47.378	17.336	35
	2008_218_09_49_17	M21A	32.756	105.494	332.335	2.813	4.2	NaN	60	NaN	36
	2008_218_09_49_17	N04	32.756	105.494	332.687	2.668	4.2	NaN	64	NaN	44
	2008_218_09_49_17	P20A	32.756	105.494	331.348	2.642	1.55	NaN	158	NaN	37
*	2008_218_09_49_17	PHWY	32.756	105.494	333.803	2.585	0.628	0.479	89.472	23.392	33
*	2008_218_09_49_17	RWWY	32.756	105.494	332.461	2.64	1.423	0.408	76.155	4.514	35
	2009_116_00_06_53	PHWY	-30.3	-178.582	236.716	3.66	1.412	1.984	70.539	26.948	33
	2009_194_18_05_01	ISCO	24.056	122.201	316.091	5.118	3.248	NaN	64.262	NaN	35
	2009_194_18_05_01	M20A	24.056	122.201	314.382	3.216	1.375	NaN	-2.841	NaN	35
*	2009_194_18_05_01	M21A	24.056	122.201	315.017	4.442	0.537	0.102	92.081	11.838	42

Best	Event Time	Station	Event Latitude	Event Longitude	Back Azimuth	Signal / Noise	δt	δt error	ϕ	ϕ error	dof
	2009_194_18_05_01	N12	24.056	122.201	314.071	3.006	1.673	NaN	2.504	NaN	65
*	2009_194_18_05_01	N23A	24.056	122.201	316	2.975	1.318	NaN	-3.387	NaN	34
	2009_194_18_05_01	O20A	24.056	122.201	314.165	3.065	1.8	NaN	141	NaN	44
	2009_194_18_05_01	O21A	24.056	122.201	314.751	2.914	1.927	2.1	-0.645	45	29
*	2009_194_18_05_01	O23A	24.056	122.201	315.922	4.129	0.882	0.98	72.143	30.637	44
	2009_194_18_05_01	O24A	24.056	122.201	316.552	2.864	1.228	NaN	1.469	NaN	32
	2009_230_21_20_47	PHWY	-26.064	-178.391	239.682	2.691	1.858	0.407	68.311	3.104	72
	2009_246_13_26_17	M21A	31.14	130.014	313.765	2.574	3.949	0.345	31.429	3.858	36
	2009_246_13_26_17	RWWY	31.14	130.014	313.867	2.615	2.55	NaN	157	NaN	23
	2009_246_13_26_17	SMCO	31.14	130.014	313.981	2.875	3.658	0.401	154.526	3.137	48
	2010_079_14_00_49	ISCO	-3.361	152.245	275.211	2.865	3.968	0.338	5.132	3.573	44
*	2010_079_14_00_49	M22A	-3.361	152.245	274.872	3.566	0.615	0.245	122.868	13.546	24
	2010_079_14_00_49	N22A	-3.361	152.245	274.854	2.522	4.2	NaN	9	NaN	31
	2010_079_14_00_49	O24A	-3.361	152.245	275.631	2.652	3.825	0.516	8.617	5.038	34
	2010_173_22_16_20	ISCO	-19.201	-177.553	243.978	2.756	3.34	0.884	72.388	3.902	36
	2010_222_23_18_31	ISCO	-14.46	167.345	257.017	3.591	2.39	1.157	83.593	4.477	25
*	2010_222_23_18_31	PHWY	-14.46	167.345	257.297	3.628	1.027	NaN	-11.631	NaN	55
	2010_223_03_35_19	PHWY	-17.403	167.814	254.755	4.186	0.472	0.199	116.716	29.692	50
	2010_228_19_35_49	ISCO	-20.799	-178.826	243.621	2.6	3.751	0.613	149.1	4.185	29
	2010_228_19_35_49	PHWY	-20.799	-178.826	243.752	4.201	3.704	0.564	149.818	1.919	72
	2011_012_21_32_53	ISCO	26.973	139.882	305.702	3.252	0.874	0.416	70.475	23.799	23
	2011_012_21_32_53	N23A	26.973	139.882	305.481	3.849	1.428	0.743	108.479	8.737	26
*	2011_012_21_32_53	PHWY	26.973	139.882	305.791	5.306	1.178	0.158	87.317	6.478	30
	2011_013_16_16_41	ISCO	-20.628	168.471	251.514	6.208	1.85	NaN	75	NaN	10
	2011_013_16_16_41	N23A	-20.628	168.471	251.497	3.684	1.668	1.141	-7.622	8.299	17
*	2011_013_16_16_41	PHWY	-20.628	168.471	251.864	5.234	0.616	0.623	123.738	46.707	13
*	2011_052_10_57_52	PHWY	-26.142	178.394	241.611	3.899	1.804	0.662	70.793	4.571	23
	2011_066_00_09_36	ISCO	-10.349	160.766	264.308	4.831	2.73	1.078	169.761	3.01	37
	2011_066_00_09_36	N23A	-10.349	160.766	264.275	2.669	2.25	NaN	1	NaN	41
	2011_066_00_09_36	PHWY	-10.349	160.766	264.655	2.979	0.65	NaN	106	NaN	34
	2011_108_13_03_02	ISCO	-34.336	179.874	234.281	6.024	2.671	1.46	57.67	2.559	27
*	2011_108_13_03_02	N23A	-34.336	179.874	234.27	4.154	2.158	0.657	62.7	3.527	31
*	2011_108_13_03_02	PHWY	-34.336	179.874	234.612	8.506	1.777	0.294	64.231	1.984	49
	2011_130_08_55_08	ISCO	-20.244	168.226	251.963	6.341	2.164	0.98	76.906	3.481	15
	2011_130_08_55_08	N23A	-20.244	168.226	251.944	3.595	0.95	NaN	-7	NaN	13
*	2011_130_08_55_08	PHWY	-20.244	168.226	252.312	8.166	0.436	0.184	120.808	31.278	20
	2011_172_02_04_15	ISCO	-11.479	165.551	260.442	2.974	2.2	NaN	86	NaN	31
*	2011_200_19_35_43	ISCO	40.081	71.41	2.322	4.247	0.884	0.222	58.597	11.789	43
	2011_200_19_35_43	N23A	40.081	71.41	2.057	3.137	0.876	1.06	63.463	37.349	54
*	2011_200_19_35_43	PHWY	40.081	71.41	2.432	4.395	1.018	0.254	67.367	7.629	38
	2011_201_22_04_59	PHWY	-10.34	162.01	263.859	2.786	1.402	2.1	2.1	45	40
	2011_210_07_42_23	ISCO	-23.801	179.751	242.29	3.043	2.513	0.603	71.593	3.983	35
	2011_210_07_42_23	N23A	-23.801	179.751	242.155	3.192	0.805	0.471	45.447	11.344	22
	2011_210_07_42_23	PHWY	-23.801	179.751	242.488	4.919	1.655	0.616	70.929	4.18	22
	2011_312_02_59_08	SMCO	27.324	125.621	314.517	2.725	3.259	0.417	69.054	3.587	31
*	2012_024_00_52_05	PHWY	-24.977	178.52	242.394	2.64	0.841	0.594	94.791	30.208	25
	2012_147_21_48_10	PHWY	26.91	140.055	305.635	2.81	1.655	0.305	100.12	4.605	36
	2012_147_21_48_10	RWWY	26.91	140.055	304.491	2.524	1.2	NaN	113	NaN	30
	2012_181_21_07_33	ISCO	43.433	84.7	352.455	2.82	0.847	1.782	62.875	64.832	51
	2012_188_02_28_22	ISCO	-14.657	167.34	256.868	5.203	1.9	NaN	81	NaN	15
	2012_188_02_28_22	PHWY	-14.657	167.34	257.151	3.997	4.15	NaN	74	NaN	39
	2012_210_20_03_56	ISCO	-4.651	153.173	273.601	3.681	3	NaN	-83	NaN	30
	2012_210_20_03_56	N23A	-4.651	153.173	273.605	3.452	4.2	NaN	4	NaN	29
	2012_224_12_23_18	PHWY	38.329	46.826	21.616	2.771	1.245	0.352	52.54	11.417	25
	2013_110_00_02_47	RWWY	30.308	102.888	333.552	2.723	4.2	NaN	70	NaN	22
	2013_111_03_22_16	ISCO	29.933	138.887	308.389	3.319	0.925	0.245	74.27	11.264	19
	2013_111_03_22_16	N23A	29.933	138.887	308.15	2.719	1.024	0.207	90.843	8.102	23
	2013_111_03_22_16	PHWY	29.933	138.887	308.445	3.326	1.322	0.155	95.538	4.151	36
	2013_111_03_22_16	RWWY	29.933	138.887	307.315	3.07	0.952	0.131	75.388	6.362	43
	2013_111_03_22_16	SMCO	29.933	138.887	307.564	3.089	2	NaN	19	NaN	32
	2013_166_11_20_36	ISCO	-33.853	179.402	234.913	2.652	3.9	NaN	149	NaN	19
*	2013_166_11_20_36	PHWY	-33.853	179.402	235.246	3.631	1.837	0.677	66.429	5.5	16
	2013_202_23_45_56	PHWY	34.512	104.262	335.456	2.935	4.015	0.274	67.618	2.203	55
	2013_202_23_45_56	RWWY	34.512	104.262	334.131	2.914	3.812	0.501	71.8	2.689	45
*	2013_240_02_54_41	ISCO	-27.754	179.62	239.418	3.531	2.32	0.388	71.032	2.687	51
*	2013_240_02_54_41	PHWY	-27.754	179.62	239.673	4.809	1.763	0.35	69.128	2.523	47
Best	**Event Time**	**Station**	**Event Latitude**	**Event Longitude**	**Back Azimuth**	**Signal / Noise**	**δt**	**δt error**	**ϕ**	**ϕ error**	**dof**

Best	Event Time	Station	Event Latitude	Event Longitude	Back Azimuth	Signal / Noise	δt	δt error	ϕ	ϕ error	dof
			Latitude	Longitude	Azimuth	Noise		error			
	1997_113_19_44_28	ISCO	13.986	144.901	293.16	2.945	3.053	1.442	23.614	3.332	38
	1997_123_16_45_44	ISCO	-33	-178	234.103	4.608	3.35	NaN	151	NaN	16
	1997_141_14_10_26	S107	-20.438	169.287	249.484	5.435	1.279	NaN	87.01	NaN	37
	1997_141_14_10_26	S111	-20.438	169.287	249.436	5.677	1.228	NaN	12.966	NaN	32

CHAPTER 3

This study has completed the majority of time-consuming research work in the form of data acquisition and signal discrimination. The Group(B) signals are worthy of focus with a multi-layer, complex anisotropy resolution technique such as that pioneered by *Menke and Levin* [2003]. Potentially, the study area may produce results of two or more layers of anisotropy south of the CB – fossil lithospheric fabric and APM. More interestingly, it may produce useful results north of the CB where the possibility of two lithospheric fabrics – upper lithosphere and the Cheyenne Slab – plus APM could be important to future seismic anisotropy studies.

REFERENCES

Buehler, J., and P. Shearer (2012), Localized imaging of the uppermost mantle with USArray Pn data, *Journal of Geophysical Research: Solid Earth (1978–2012)*, *117*(B9).

Chamberlain, K. R., C. D. Frost, and B. R. Frost (2003), Early Archean to Mesoproterozoic evolution of the Wyoming Province: Archean origins to modern lithospheric architecture, *Canadian Journal of Earth Sciences*, *40*(10), 1357-1374.

Crotwell, H. P. O., T. J.; Ritsema, J. (1999), The TauP Toolkit: Flexible seismic travel-time and ray-path utilities, edited, University of South Carolina.

Hess, H. H. (1964), Seismic Anisotropy of the Uppermost Mantle under Oceans, *Nature*, *203*(4945), 629-631.

Karlstrom, K., and M. Williams (2006), Nature of the middle crust—Heterogeneity of structure and process due to pluton-enhanced tectonism: An example from Proterozoic rocks of the North American Southwest, *Evolution and differentiation of the continental crust*, 268-295.

Larson, K. M., J. T. Freymueller, and S. Philipsen (1997), Global plate velocities from the Global Positioning System, *Journal of Geophysical Research: Solid Earth (1978–2012)*, *102*(B5), 9961-9981.

Long, M., and P. Silver (2009), Shear Wave Splitting and Mantle Anisotropy: Measurements, Interpretations, and New Directions, *Surv Geophys*, *30*(4-5), 407-461, doi:10.1007/s10712-009-9075-1.

Menke, W., and V. Levin (2003), The cross-convolution method for interpreting SKS splitting observations, with application to one and two-layer anisotropic earth models, *Geophysical Journal International*, *154*(2), 379-392, doi:10.1046/j.1365-246X.2003.01937.x.

Nesse, W. D. (2004), *Introduction to optical mineralogy*, Oxford University Press, New York.

Pesonen, L. J., S. Å. Elming, S. Mertanen, S. Pisarevsky, M. S. D'Agrella-Filho, J. G. Meert, P. W. Schmidt, N. Abrahamsen, and G. Bylund (2003), Palaeomagnetic configuration of continents during the Proterozoic, *Tectonophysics*, *375*(1–4), 289-324, doi:http://dx.doi.org/10.1016/S0040-1951(03)00343-3.

Schutt, D., E. D. Humphreys, and K. Dueker (1998), Anisotropy of the Yellowstone hot spot wake, eastern Snake River Plain, Idaho, in *Geodynamics of Lithosphere & Earth's Mantle*, edited, pp. 443-462, Springer.

Silver, P. G., and W. W. Chan (1991), Shear wave splitting and subcontinental mantle deformation, *Journal of Geophysical Research: Solid Earth*, *96*(B10), 16429-16454, doi:10.1029/91JB00899.

Sullivan, W., and R. Beane (2013), A new view of an old suture zone: Evidence for sinistral transpression in the Cheyenne belt, *Geological Society of America Bulletin*, *125*(7-8), 1319-1337.

Turner, F. J. (1942), Preferred orientation of olivine crystals in peridotites, with special reference to New Zealand examples, *Trans. Roy. Soc. NZ*, *72*(3), 280-300.

Tyson, A. R., E. Morozova, K. Karlstrom, K. C. S. S. K. Dueker, and C. Foster (2002), Proterozoic Farwell Mountain–Lester Mountain suture zone, northern Colorado: Subduction flip and progressive assembly of arcs, *Geology*, *30*(10), 943-946.

Verma, R. K. (1960), ELASTICITY OF SOME HIGH-DENSITY CRYSTALS, *Journal of Geophysical Research*, *65*(2), 757-766, doi:10.1029/JZ065i002p00757.

Vinnik, L., G. Kosarev, and L. Makeeva (1984), Lithosphere anisotropy from the observation of SKS and SKKS waves, *Doklady Akademii Nauk SSSR*, *278*(6), 1335-1339.

Whitmeyer, S. J., and K. E. Karlstrom (2007), Tectonic model for the Proterozoic growth of North America, *Geosphere*, *3*(4), 220-259, doi:10.1130/ges00055.1.

Wolfe, C. J., and P. G. Silver (1998), Seismic anisotropy of oceanic upper mantle: Shear wave splitting methodologies and observations, *Journal of Geophysical Research: Solid Earth (1978–2012)*, *103*(B1), 749-771.

Wüstefeld, A., G. Bokelmann, G. Barruol, and J.-P. Montagner (2009), Identifying global seismic anisotropy patterns by correlating shear-wave splitting and surface-wave data, *Physics of the Earth and Planetary Interiors*, *176*(3–4), 198-212, doi:http://dx.doi.org/10.1016/j.pepi.2009.05.006.

Yuan, H., and K. Dueker (2005), Upper mantle tomographic Vp and Vs images of the Rocky Mountains in Wyoming, Colorado and New Mexico: Evidence for a thick heterogeneous chemical lithosphere, *Geophysical Monograph Series*, *154*, 329-345.